Available online at www.sciencedirect.com
ScienceDirect
Comput. Methods Appl. Mech. Engrg. 309 (2016) 325–363
Computer methods in applied mechanics and engineering
www.elsevier.com/locate/cma

The buckling sphere
A symbiosis of mechanics and geometry

H.A. Mang[a,b,*], S. Pavlicek[a], X. Jia[b]

[a] *Institute for Mechanics of Materials and Structures, Technical University of Vienna, Karlsplatz 13/202, 1040 Vienna, Austria*
[b] *Tongji University, Siping Road 1239, Shanghai, China*

Received 1 March 2016; received in revised form 25 May 2016; accepted 26 May 2016
Available online 15 June 2016

Abstract

The basis of this work is a novel symbiosis of mechanics of solids and spherical geometry to quantify and illustrate the variation of the "non-membrane" percentage of the strain energy in the prebuckling region of linear elastic beams, arches, plates and shells, and structures assembled of such one-dimensional and two-dimensional members. The zenith angle of an arbitrary point of a specific curve on an octant of the unit sphere, called buckling sphere, is related to this energy percentage. For the limiting case of buckling from a membrane stress state this curve degenerates to a point, characterized by zero values of both spherical coordinates. For all other stress states the azimuth angle increases with the proportionally increasing load. Its magnitude at the stability limit correlates with a global quantity that depends on both the "non-membrane" deformations and the stiffness of the structure at incipient buckling. The azimuth angle is computed with the help of the so-called consistently linearized eigenproblem, which is solved by means of the Finite Element Method. This eigenvalue problem is the basis for a hypothesis for the "non-membrane" percentage of the strain energy. In the theoretical part of the paper, the concept of the buckling sphere is presented. The subsequent numerical investigation consists of four examples, referring to buckling from a membrane stress state, a pure bending stress state, and a general stress state. The practical motive for this research is the intention to investigate the influence of "non-membrane" action just before buckling on the initial postbuckling behavior of elastic structures.

Keywords: Buckling sphere; Consistently linearized eigenvalue problem; Spherical geometry; Membrane pole; Bending equator

1. Prolog

Geometry has a long tradition in the history of man, which goes beyond the sciences and engineering. Fig. 1 shows that this tradition also includes medieval theology.

The basis of this work is a novel symbiosis of solid mechanics and spherical geometry to quantify and illustrate the variation of the "non-membrane" percentage of the strain energy and of its membrane complement, respectively, in

* Corresponding author at: Institute for Mechanics of Materials and Structures, Technical University of Vienna, Karlsplatz 13/202, 1040 Vienna, Austria. Fax: +43 15880120299.
E-mail address: herbert.mang@tuwien.ac.at (H.A. Mang).

http://dx.doi.org/10.1016/j.cma.2016.05.033

Fig. 1. God as geometer, from Bible Moralisée, France, around 1220–1230, Austrian National Library, Vienna.

the prebuckling region, including the stability limit, of linear elastic beams, arches, plates and shells, and assemblies of such one-dimensional and two-dimensional members. Although the term "extensional" would fit beams and arches better than the term "membrane", for convenience's sake the latter is collectively used in this work. The practical motive for this long-standing research is the intention to investigate the influence of "non-membrane" action before buckling on the initial prebuckling behavior of such structures.

2. Restrictions

This work is restricted to static, conservative, and proportional loading of perfect structures consisting of one-dimensional and two-dimensional members made of linear elastic material. These restrictions are irrelevant to the motive for this publication, which follows from its title.

3. Organization of the paper

In Section 4, the concept of the buckling sphere is introduced. Section 5 contains a literature review. Section 6 is devoted to the limiting case of buckling from a membrane stress state. Section 7 deals with a hypothesis for the "non-membrane" percentage of the strain energy. It is based on a particular linear eigenvalue problem that plays a key role in this work. The purpose of Section 8 is to underscore the outstanding features of a specific eigenpair of this eigenvalue problem. Section 9 contains results from a numerical investigation, which includes buckling from a membrane stress state, a pure bending stress state, and a general stress state. Conclusions drawn from this work are listed in Section 10. Appendix A contains derivations of differential geometric quantities. The topic of Appendix B is the numerical realization of the proposed concept in the framework of the Finite Element Method (FEM). Appendix C deals with the numerical determination of the aforesaid eigenpair, i.e. with a detail of Appendix B.

4. Buckling sphere

The response of a structure is usually displayed in load–displacement diagrams, which may include bifurcation points and/or snap-through points, see e.g. Figs. 9(a), 18, and 23(a) in this work. Sometimes an estimated value of the buckling load, in the form of a dimensionless load parameter, is plotted versus the actual load, see e.g. Figs. 9(b), 13(a), 20(a), and 23(b) in this work.

In accord with the title of and the motive for this work, another procedure is proposed in this paper. Its characteristic feature is an octant of the unit sphere, see Fig. 2, for convenience's sake called *buckling sphere*. $\mathbf{e}_x$, $\mathbf{e}_y$, $\mathbf{e}_z$ denote unit vectors in the respective coordinate directions. P is a point on a surface curve, described by the vertex of the unit vector

$$\mathbf{a}(\theta(\lambda), \varphi(\lambda)) = \left\{ \begin{matrix} \sin\theta\ \cos\varphi \\ \sin\theta\ \sin\varphi \\ \cos\theta \end{matrix} \right\}, \tag{1}$$

where $\theta(\lambda)$ and $\varphi(\lambda)$ are the two spherical coordinates, which depend on the dimensionless load parameter λ. They follow from

$$\sin^2\theta = \frac{U - U_M}{U}, \tag{2}$$

where U_M is the membrane energy, which is part of the strain energy U, and from

$$\cos\varphi = \mathbf{v}_{10}^* \cdot \mathbf{v}_1^*, \quad \mathbf{v}_{10}^* := \mathbf{v}_1^*(0); \ \|\mathbf{v}_1^*\| = 1, \tag{3}$$

respectively. $\mathbf{v}_1^*$ is a specific eigenvector of

$$\boxed{\left[\widetilde{\mathbf{K}}_T(\lambda) + (\lambda^* - \lambda)\dot{\widetilde{\mathbf{K}}}_T(\lambda)\right] \cdot \mathbf{v}^* = \mathbf{0}}, \tag{4}$$

representing the mathematical formulation of the so-called *consistently linearized eigenproblem*, abbreviated as CLE. $\widetilde{\mathbf{K}}_T(\lambda)$ denotes the tangent stiffness matrix in the framework of the FEM. The tilde above $\mathbf{K}_T$ indicates that the matrix $\widetilde{\mathbf{K}}_T$ refers to an equilibrium state. Noting that $\dot{} := \mathrm{d}/\mathrm{d}\lambda$, $\dot{\widetilde{\mathbf{K}}}_T$ is the derivative of $\widetilde{\mathbf{K}}_T$ with respect to λ. Because of its special mathematical properties at the stability limit, the eigenpair $(\lambda_1^* - \lambda, \mathbf{v}_1^*)$ stands out from the remaining $N-1$ eigenpairs of a system with N degrees of freedom, see Section 8. Therefore, it is referred to as the *fundamental eigenpair*. The CLE was first used by Helnwein [1], albeit for a completely different purpose.

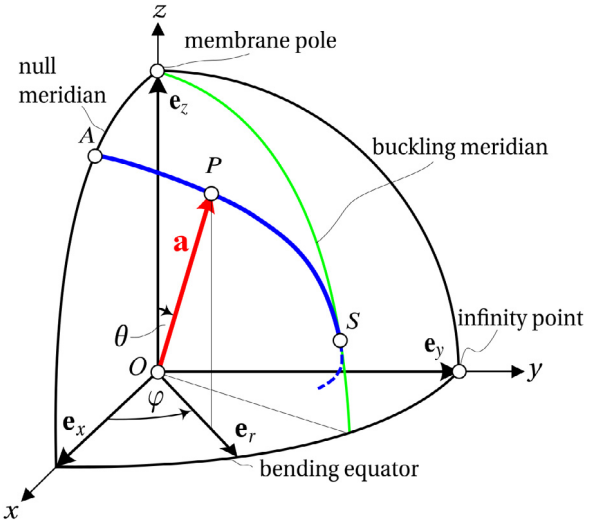

Fig. 2. Buckling sphere.

The designations *membrane pole* and *bending equator* in Fig. 2 follow from specializing Eq. (2) for the energetical limiting cases

$$U_M(\lambda) = U(\lambda) \implies \theta(\lambda) = 0 \tag{5}$$

and

$$U_M(\lambda) = 0 \implies \theta(\lambda) = \frac{\pi}{2}. \tag{6}$$

The former is based on a membrane stress state in the prebuckling region and the latter on a "non-membrane" stress state, a special case of which is a pure bending stress state. For convenience's sake the equator is named after this special case.

The surface curve starts at point A, which is located on the *null meridian*, see Fig. 2. This designation follows from specializing Eq. (3) for $\lambda = 0$, resulting in

$$\cos\varphi(0) = \mathbf{v}_{10}^{*} \cdot \mathbf{v}_{10}^{*} = 1 \implies \varphi(0) = 0. \tag{7}$$

Fig. 3 shows the cross-section $\varphi = const.$ of the buckling sphere. The decisive part of the surface curve ends at the stability limit S, see Fig. 2. The value of λ at S is denoted as λ_S. At S, the surface curve is tangent to the meridian, called *buckling meridian*. This is the consequence of $\varphi(\lambda)$ becoming a maximum at the stability limit, see Section 9. The monotonic increase of $\varphi(\lambda)$ in the prebuckling regime was one of the reasons for defining the azimuth angle according to Eq. (3).

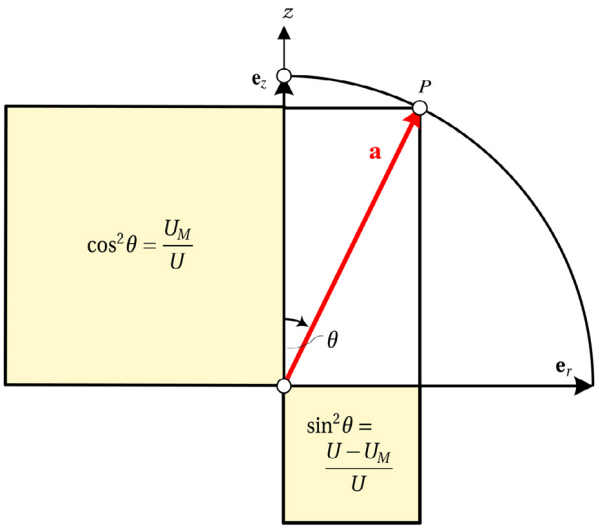

Fig. 3. Cross-section $\varphi = const.$ of the buckling sphere.

A practical argument why the illustration of the vector function $\mathbf{a}(\theta, \varphi)$ on the buckling sphere is preferred to a θ–φ diagram is its superior graphicness. This argument is supported e.g. by Fig. 3. A more basic argument for this preference is the indispensable role of this vector function in the following explanation of the sufficiency of an octant of the unit sphere for this research. This argument is supported by Figs. 4 and 5.

The mechanical meaning of the term *infinity point* in Fig. 2 follows from the unphysical situation

$$U(\lambda_S) = \infty, \qquad U_M(\lambda_S) \neq \infty, \tag{8}$$

resulting in

$$\sin^2\theta(\lambda_S) = \frac{U(\lambda_S) - U_M(\lambda_S)}{U(\lambda_S)} = 1 \implies \theta(\lambda_S) = \frac{\pi}{2}. \tag{9}$$

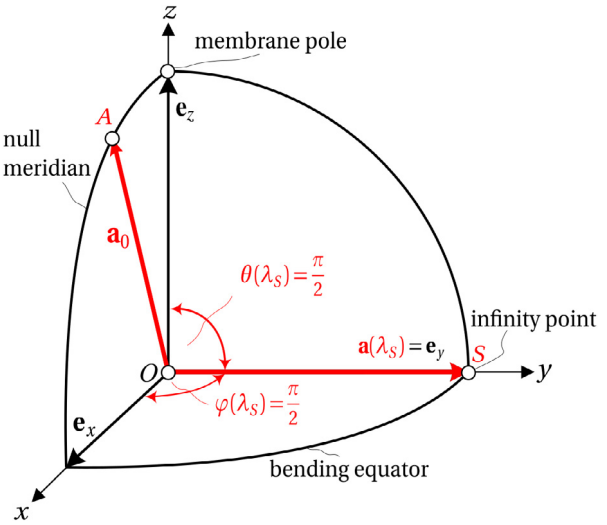

Fig. 4. Bar subjected to an eccentric compressive force: $\mathbf{a}_0$ and $\mathbf{a}(\lambda_S) = \mathbf{e}_y$ according to second-order theory.

The same result is obtained for buckling from a pure bending stress state, characterized by Eq. (6). A distinctive feature of these two limiting cases is the value of $\varphi(\lambda_S)$. For a pure bending stress state,

$$0 < \cos\,\varphi(\lambda_S) = \mathbf{v}_{10}^* \cdot \mathbf{v}_1^*(\lambda_S) < 1 \implies 0 < \varphi(\lambda_S) < \frac{\pi}{2}, \tag{10}$$

see Fig. 15. For the unphysical limiting situation according to Eq. (8), however,

$$\cos\,\varphi(\lambda_S) = \mathbf{v}_{10}^* \cdot \mathbf{v}_1^*(\lambda_S) = 0 \implies \varphi(\lambda_S) = \frac{\pi}{2}, \tag{11}$$

see Fig. 4. An example for this purely academic case is an elastic bar, subjected to an eccentric compressive force, which is analyzed by means of second-order theory beyond the region of validity of this theory [2]. For this example, λ_S is equal to the Euler load, which obviously does not depend on the value of the eccentricity of the force. This requires

$$\mathbf{a}_0 \cdot \mathbf{a}(\lambda_S) = 0, \qquad \mathbf{a}_0 := \mathbf{a}(0), \tag{12}$$

independent of the position of $\mathbf{a}_0$ in the $\mathbf{e}_x$–$\mathbf{e}_z$ plane, which depends on the eccentricity of the compressive force. Thus,

$$\mathbf{a}(\lambda_S) = \mathbf{e}_y, \tag{13}$$

see Fig. 4. Consequently, also $\mathbf{v}_{10}^* \cdot \mathbf{v}_1^*(\lambda_S)$ cannot depend on the position of $\mathbf{a}_0$ in this plane, resulting in Eq. (11).

$\theta(\lambda_S) = \pi/2$ is a necessary condition for $\varphi(\lambda_S) = \pi/2$. Thus, the combination $\varphi(\lambda) = \pi/2$ and $0 < \theta(\lambda) < \pi/2$ refers to the prebuckling region. This raises the question of the type of stability limit with $\varphi(\lambda_S) > \pi/2$. Fig. 5 serves the purpose to answer this question. Anticipating numerical results, presented in Section 9, it shows roughly sketched φ–λ diagrams for four different types of loss of stability. They are characterized by four different combinations of φ and $\mathrm{d}\varphi/\mathrm{d}\lambda$ at the stability limit. For all of them, $\mathrm{d}\varphi(\lambda_S) = 0$. Fig. 5(a) refers to bifurcation buckling, where

$$0 \le \varphi(\lambda_S) < \frac{\pi}{2}, \qquad \frac{\mathrm{d}\varphi}{\mathrm{d}\lambda}(\lambda_S) = 0, \tag{14}$$

see Figs. 22 and 25 and Eq. (111). Fig. 5(b) refers to snap-through, where

$$0 \le \varphi(\lambda_S) < \frac{\pi}{2}, \qquad \frac{\mathrm{d}\varphi}{\mathrm{d}\lambda}(\lambda_S) = \frac{0}{0} \implies 0 \le \frac{\mathrm{d}\varphi}{\mathrm{d}\lambda}(\lambda_S) < \infty, \tag{15}$$

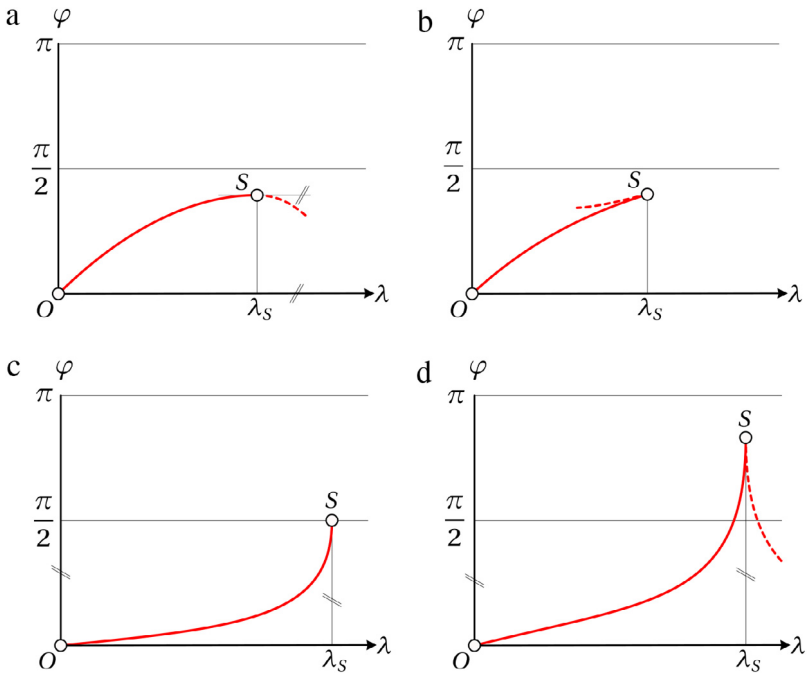

Fig. 5. φ–λ diagrams for (a) bifurcation buckling, (b) snap-through, (c) infinity-point "buckling", (d) saddle-point buckling.

see Figs. 17 and 21 and Eq. (101). Fig. 5(c) is related to the academic limiting case with the aforementioned *infinity point*, called *infinity-point "buckling"*, for which

$$\varphi(\lambda_S) = \frac{\pi}{2}, \qquad \frac{\mathrm{d}\varphi}{\mathrm{d}\lambda}(\lambda_S) = \frac{0}{0} = \infty, \tag{16}$$

see Fig. 4 and Eq. (11). Fig. 5(d) refers to bifurcation buckling from a saddle point of the load–displacement diagrams, called *saddle-point buckling*. For this limiting case,

$$\frac{\pi}{2} < \varphi(\lambda_S) < \pi, \qquad \frac{\mathrm{d}\varphi}{\mathrm{d}\lambda}(\lambda_S) = \frac{0}{0} = \infty. \tag{17}$$

This type of loss of stability is the only one with a stability limit outside the octant of the unit sphere, shown in Figs. 2 and 4. In view of the practical insignificance of this limiting case, which is usually characterized by large deformations at the stability limit, combined with imperfection insensitivity of the initial postbuckling behavior of the structure, the restriction of the present work to this octant is justified.

5. Literature review

This work is embedded in a research project, sponsored by the Austrian Science Fund [3]. The idea of visualizing the variation of the membrane percentage of the strain energy in the prebuckling regime of linear elastic structures by means of a symbiosis of mechanics and geometry was an important motivation for tackling this project. An essential element of this symbiosis is the CLE. It belongs to a class of linear eigenvalue problems, which contain the tangent stiffness matrix as one of the two coefficient matrices and different real symmetric matrices as the other one. Such linear eigenvalue problems have been frequently used to estimate the stability limit on nonlinear load–displacement paths by means of the FEM, see e.g. [4–6]. The respective eigenvalue analyses are called *accompanying linear eigenvalue analyses*. The CLE was originally used to compute *ab initio* estimates of stability limits on nonlinear load–displacement paths [1].

A paper on bifurcation buckling from a membrane stress state [7] and one on FE analysis of buckling from special prebuckling stress states [8] are relevant to the present work insofar as they contain numerical results, which were obtained by the CLE. Specific characteristic features of these results for the special case of buckling from a membrane

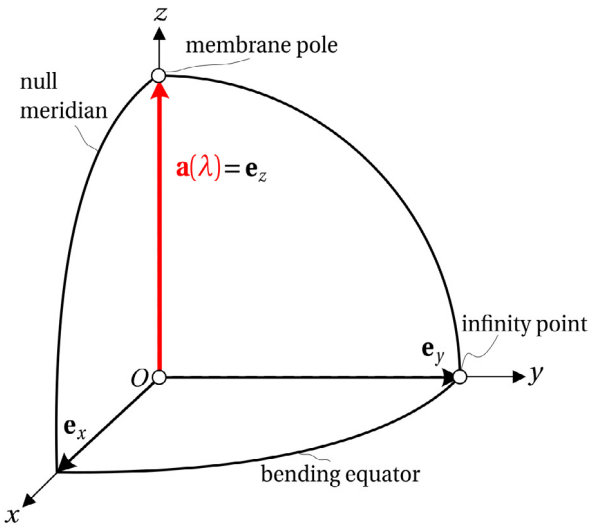

Fig. 6. Membrane stress state.

stress state prompted the authors to explore the observed situation on a very much larger scale in the framework of the aforementioned research project.

6. Buckling from a membrane stress state

For a membrane stress state in the prebuckling regime,

$$\mathbf{a}(\theta(\lambda), \varphi(\lambda)) = \begin{Bmatrix} 0 \\ 0 \\ 1 \end{Bmatrix}, \tag{18}$$

see Fig. 6. Based on the constancy of $\mathbf{a}$, the constancy of $\mathbf{v}_1^*$ is hypothesized, i.e.

$$\mathbf{v}_1^*(\lambda) = \mathbf{v}_{10}^*. \tag{19}$$

Making use of this hypothesis in Eq. (3) gives

$$\cos\,\varphi(\lambda) = 1 \implies \varphi(\lambda) = 0. \tag{20}$$

Provided the hypothesis can be verified, $\varphi(\lambda) = 0$ is a necessary and sufficient condition for $\theta(\lambda) = 0$.

In the following, it will be shown that the CLE can produce a constant eigenvector that corresponds to a nonlinearly varying eigenvalue. The starting point of this task is the specialization of

$$\left[\widetilde{\mathbf{K}}_T(\lambda) + (\lambda^{\triangle}(\lambda) - \lambda)\mathbf{B}(\lambda)\right] \cdot \mathbf{v}^{\triangle}(\lambda) = \mathbf{0}, \tag{21}$$

where $\mathbf{B}(\lambda)$ is an arbitrary real symmetric matrix, for the eigenpair $(\lambda_1^{\triangle}(\lambda) - \lambda,\ \mathbf{v}_1^{\triangle}(\lambda))$, characterized by

$$\lambda_1^{\triangle}(\lambda_S) = \lambda_1^*(\lambda_S) = \lambda_S \tag{22}$$

and

$$\mathbf{v}_1^{\triangle}(\lambda_S) = \mathbf{v}_1^*(\lambda_S); \tag{23}$$

$\lambda_1^*(\lambda_S)$ and $\mathbf{v}_1^*(\lambda_S)$ are connected with the CLE. This gives

$$\left[\widetilde{\mathbf{K}}_T(\lambda) + (\lambda_1^{\triangle}(\lambda) - \lambda)\mathbf{B}(\lambda)\right] \cdot \mathbf{v}_1^{\triangle}(\lambda) = \mathbf{0}. \tag{24}$$

The superscript Δ serves as a distinctive feature of the eigenpair $(\lambda_1^{\Delta}(\lambda) - \lambda, \mathbf{v}_1^{\Delta}(\lambda))$ from the fundamental eigenpair $(\lambda_1^{*}(\lambda) - \lambda, \mathbf{v}_1^{*}(\lambda))$ of the CLE. Derivation of Eq. (24) with respect to λ results in

$$[\tilde{\dot{\mathbf{K}}}_T + (\dot{\lambda}_1^{\Delta} - 1)\mathbf{B} + (\lambda_1^{\Delta} - \lambda)\dot{\mathbf{B}}] \cdot \mathbf{v}_1^{\Delta} + [\widetilde{\mathbf{K}}_T + (\lambda_1^{\Delta} - \lambda)\mathbf{B}] \cdot \dot{\mathbf{v}}_1^{\Delta} = \mathbf{0}. \tag{25}$$

Since the eigenvectors of a linear eigenvalue problem represent a complete basis, $\dot{\mathbf{v}}_1^{\Delta}$ can be expressed in terms of $\mathbf{v}_j^{\Delta}$, $j = 2, 3, \ldots, N$. Thus,

$$\dot{\mathbf{v}}_1^{\Delta} = \sum_{j=2}^{N} c_{1j}^{\Delta} \mathbf{v}_j^{\Delta}. \tag{26}$$

Because of $\|\mathbf{v}_1^{\Delta}\| = 1$, $\mathbf{v}_1^{\Delta}$ does not contribute to $\dot{\mathbf{v}}_1^{\Delta}$. Premultiplication of Eq. (25) by $\mathbf{v}_j^{\Delta}$ and consideration of the orthogonality relations

$$\mathbf{v}_j^{\Delta} \cdot \widetilde{\mathbf{K}}_T \cdot \mathbf{v}_1^{\Delta} = 0, \qquad \mathbf{v}_j^{\Delta} \cdot \mathbf{B} \cdot \mathbf{v}_1^{\Delta} = 0, \quad j = 2, 3, \ldots, N, \tag{27}$$

which follow from Eq. (24), results in the following expression for c_{1j}^{Δ}:

$$c_{1j}^{\Delta} = -\frac{\mathbf{v}_j^{\Delta} \cdot [\tilde{\dot{\mathbf{K}}}_T + (\lambda_1^{\Delta} - \lambda)\dot{\mathbf{B}}] \cdot \mathbf{v}_1^{\Delta}}{\mathbf{v}_j^{\Delta} \cdot [\widetilde{\mathbf{K}}_T + (\lambda_1^{\Delta} - \lambda)\mathbf{B}] \cdot \mathbf{v}_j^{\Delta}}. \tag{28}$$

Specialization of Eq. (21) for the eigenpair $(\lambda_j^{\Delta}(\lambda) - \lambda,\ \mathbf{v}_j^{\Delta}(\lambda))$ gives

$$\left[\widetilde{\mathbf{K}}_T(\lambda) + (\lambda_j^{\Delta}(\lambda) - \lambda)\mathbf{B}(\lambda)\right] \cdot \mathbf{v}_j^{\Delta}(\lambda) = \mathbf{0}. \tag{29}$$

Premultiplication of Eq. (29) by $\mathbf{v}_j^{\Delta}(\lambda)$ in order to eliminate $\mathbf{v}_j^{\Delta} \cdot \widetilde{\mathbf{K}}_T \cdot \mathbf{v}_j^{\Delta}$ in Eq. (28) yields

$$c_{1j}^{\Delta} = -\frac{\mathbf{v}_j^{\Delta} \cdot \tilde{\dot{\mathbf{K}}}_T \cdot \mathbf{v}_1^{\Delta} + (\lambda_1^{\Delta} - \lambda)\ \mathbf{v}_j^{\Delta} \cdot \dot{\mathbf{B}} \cdot \mathbf{v}_1^{\Delta}}{(\lambda_1^{\Delta} - \lambda_j^{\Delta})\ \mathbf{v}_j^{\Delta} \cdot \tilde{\dot{\mathbf{K}}}_T \cdot \mathbf{v}_j^{\Delta}}. \tag{30}$$

A constant eigenvector implies

$$\dot{\mathbf{v}}_1^{\Delta}(\lambda) = \mathbf{0}. \tag{31}$$

As follows from Eqs. (26) and (31), this requires

$$c_{1j}^{\Delta}(\lambda) = 0. \tag{32}$$

Satisfaction of Eq. (32) for arbitrary values of λ requires disintegration of the vanishing numerator in the expression for c_{1j}^{Δ}, see Eq. (30), into

$$\mathbf{v}_j^{\Delta} \cdot \tilde{\dot{\mathbf{K}}}_T \cdot \mathbf{v}_1^{\Delta} = 0, \qquad \mathbf{v}_j^{\Delta} \cdot \dot{\mathbf{B}} \cdot \mathbf{v}_1^{\Delta} = 0. \tag{33}$$

A necessary condition for satisfaction of these two relations is

$$\boxed{\mathbf{B} = \tilde{\dot{\mathbf{K}}}_T}. \tag{34}$$

It guarantees satisfaction of Eq. (33.1). Substitution of Eq. (34) into Eq. (24) and replacement of the eigenpair $(\lambda_1^{\Delta}(\lambda) - \lambda,\ \mathbf{v}_1^{\Delta}(\lambda))$ by the fundamental eigenpair of the CLE gives

$$\boxed{\left[\widetilde{\mathbf{K}}_T(\lambda) + (\lambda_1^{*}(\lambda) - \lambda)\tilde{\dot{\mathbf{K}}}_T(\lambda)\right] \cdot \mathbf{v}_1^{*}(\lambda) = \mathbf{0}}. \tag{35}$$

By analogy,

$$c_{1j}^{*} = -(\lambda_1^{*} - \lambda)\frac{\mathbf{v}_j^{*} \cdot \overset{\cdot\cdot}{\tilde{\mathbf{K}}}_T \cdot \mathbf{v}_1^{*}}{(\lambda_1^{*} - \lambda_j^{*})\, \mathbf{v}_j^{*} \cdot \dot{\tilde{\mathbf{K}}}_T \cdot \mathbf{v}_j^{*}} \tag{36}$$

replaces $c_{1j}^{\triangle}$ according to Eq. (30). Thus, satisfaction of

$$\dot{\mathbf{v}}_1^{*}(\lambda) = \sum_{j=2}^{N} c_{1j}^{*} \mathbf{v}_j^{*} = \mathbf{0} \tag{37}$$

requires that $\mathbf{v}_1^{*}(\lambda) = \mathbf{v}_{10}^{*}$ satisfies the condition

$$\boxed{\mathbf{v}_j^{*} \cdot \overset{\cdot\cdot}{\tilde{\mathbf{K}}}_T \cdot \mathbf{v}_1^{*} = 0}. \tag{38}$$

Contrary to the *mathematical orthogonality conditions*

$$\mathbf{v}_j^{*} \cdot \widetilde{\mathbf{K}}_T \cdot \mathbf{v}_1^{*} = 0, \qquad \mathbf{v}_j^{*} \cdot \dot{\tilde{\mathbf{K}}}_T \cdot \mathbf{v}_1^{*} = 0, \tag{39}$$

which follow from Eq. (35), Eq. (38) represents a *physical orthogonality condition*. A special case of satisfaction of Eq. (38) is

$$\overset{\cdot\cdot}{\tilde{\mathbf{K}}}_T(\lambda) = \mathbf{0}. \tag{40}$$

It refers to linear stability analyses [9]. They are characterized by a linear decrease of the fundamental eigenvalue $\lambda_1^{*}(\lambda) - \lambda$ of the CLE in the prebuckling regime to zero at the bifurcation point. Incidentally, such analyses and linear prebuckling paths need not be mutually conditional [10]. Seen from a theoretical point of view, the applicability of linear stability analyses is restricted to special forms of buckling from a membrane stress state. Hence, it is plausible that Eq. (38), which is based on the constancy of $\mathbf{v}_1^{*}$, is a general condition for buckling from a membrane stress state. This argument will be verified numerically in Section 9.

7. CLE-based hypothesis for $(U - U_M)/U$

Ab initio there were speculations that the CLE would permit determination of $(U - U_M)/U$. They were nourished by numerical evidence of the constancy of $\mathbf{v}_1^{*}$ for the limiting case of a membrane stress state [7], [8]. These speculations were the driving force behind the previously mentioned research project [3]. If they proved right, the CLE could also be used for computation of the zenith angle θ, see Eq. (2), of $\mathbf{a}(\theta(\lambda),\ \varphi(\lambda))$. The motive for this form of computation of θ was a symbiosis of mechanics and geometry to the greatest possible extent. This is, of course, a rather theoretical goal, because $(U - U_M)/U$ can alternatively and more conveniently be computed in a conventional manner in the framework of the FEM, see Appendix B.3.

The aforementioned speculations have led to a CLE-based hypothesis for $(U - U_M)/U$, the mathematical formulation of which reads

$$\boxed{\frac{U - U_M}{U} = \sqrt{\rho^2 + c^2\left(1 - \rho^2\right)}}, \tag{41}$$

where

$$\rho \equiv \frac{1}{\kappa} = -\mathbf{n} \cdot \mathbf{v}_1^{*}, \quad 0 \le \rho(\lambda) < 1. \tag{42}$$

$\kappa(\lambda)$ is the curvature of a fictitious curve on the surface of the unit sphere, described by the vertex of the fundamental eigenvector $\mathbf{v}_1^{*}(\lambda)$, which is a unit vector, and $\mathbf{n}$ denotes the principal normal vector, which is also a unit vector. Appendix A contains the derivation of Eq. (42). The adjective *fictitious* should make the fact clearer that $\mathbf{v}_1^{*}(\lambda)$ is not a vector in a physical sense, uniquely determined by its components in the directions of the three coordinate axes of a

Cartesian system of reference, and conversely. Such a vector is a special case of an N-dimensional vector in a matric sense, which represents an ordered set of N quantities [11], as is the case in the FEM. A further argument for the term *fictitious curve* is the fact that $\rho(\lambda)$ does not depend on the position of $\mathbf{v}_1^*(\lambda)$ relative to the three coordinate axes. Not least, this term should help avoiding a confusion of $\mathbf{v}_1^*(\lambda)$ with $\mathbf{a}(\lambda)$. In this context the CLE-based hypothesis for $(U - U_M)/U$ may also be seen as a vehicle for a dimensional reduction from N to 3.

$c(\lambda)$ is obtained as

$$c = \frac{v\lambda_{,\xi}}{\lambda_1^* - \lambda}, \tag{43}$$

where

$$v = \|\mathbf{v}_{1,\xi}^*\|, \quad {}_{,\xi} := \frac{\mathrm{d}}{\mathrm{d}\xi}, \tag{44}$$

with ξ as a displacement-dependent parameter that will be defined in Section 8. Eq. (43) follows from an equation of definition for $c^2(1 - \rho^2)$, see Eq. (A.16) in Appendix A, that accounts for the twist of the fictitious surface curve. Appendix A contains the derivation of Eq. (43) with the help of the 2nd *Frenet* formula.

Specialization of Eq. (43) for the limiting case of a membrane stress state in the prebuckling regime, characterized by

$$v(\lambda) = 0, \tag{45}$$

following from Eqs. (19) and (44), yields

$$c(\lambda) = 0, \tag{46}$$

which is the lower bound of $c(\lambda)$. Substitution of Eqs. (5) and (46) into Eq. (41) results in

$$\frac{U - U_M}{U} = 0 \implies \rho(\lambda) = 0, \tag{47}$$

underscoring the interpretation of the vertex of a constant unit vector $\mathbf{v}_1^*$ as a degenerate circle on the surface of the unit sphere. As shown in Appendix A, see Eq. (A.15), $v = 0$ and $\rho = 0$ are characteristic features of a singular point of $\mathbf{v}_1^*(\lambda)$. Consequently, the present limiting case solely consists of such a point. Provided the hypothesized constancy of $\mathbf{v}_1^*(\lambda)$ for this limiting case can be verified numerically by confirming previous numerical evidence, the hypothesis for $(U - U_M)/U$, see Eq. (41), is verified for this special case. For the limiting case of buckling from a pure bending stress state, this hypothesis requires

$$c(\lambda) = 1, \tag{48}$$

which is the upper bound of $c(\lambda)$.

In Section 9.2, the condition

$$0 \leq \rho(\lambda) < 1, \tag{49}$$

see Eq. (42), will be checked numerically for this limiting case. If, contrary to the semi-open interval for $\rho(\lambda)$, this quantity could become equal to 1 for an arbitrary value of λ, this would entail $1 - \rho^2 = 0$ and, furthermore, $U_M = 0$ for that value, as follows from Eq. (41). However, U_M is either zero for all values of λ in the prebuckling regime or for none. To conclude from this that $U_M = 0$ implies $\rho = 1$ for all values of λ would be incorrect. It would result in the vanishing of the second term in the expression on the right-hand side of Eq. (41), independent of $c(\lambda)$, see Eq. (43). In other words, $v(\lambda) = 0$ would not be necessary for the vanishing of this term. This would raise the question of its indispensability in the hypothesis for $(U - U_M)/U$, see Eq. (41). Indeed, if both limiting cases, i.e. $U_M = U$ and $U_M = 0$, could be treated without this term, it would not be illogical to suspect that also the general case, i.e. $0 < (U - U_M)/U < 1$, can be treated in this way. In the end, this would obscure the different roles of the vectors $\mathbf{a}$ and $\mathbf{v}_1^*$ in this research.

Eq. (41) contains first-order and second-order derivatives of $\mathbf{v}_1^*(\lambda)$, see Appendix A. They are approximated by finite-difference expressions, see Appendix B.2. $\mathbf{v}_1^*(\lambda)$ is part of the numerical solution of the CLE, see Appendix B.1.

In general, this solution is based on a finite-difference approximation of $\overset{\cdot\cdot}{\widetilde{\mathbf{K}}}_T(\lambda)$, see Appendix B.1.3. Bearing all this in mind, it becomes obvious that determination of a suitable approximation of Eq. (48) is a challenging task.

8. Outstanding features of the fundamental eigenpair of the CLE

In order to underscore the singular role of the fundamental eigenpair of the CLE, λ_1^*–λ diagrams are compared with λ_j^*–λ diagrams, where $j \neq 1$. Fig. 7, taken from [1], shows such diagrams. They refer to two shallow cylindrical panels, which are simply supported along their straight edges and free at the curved edges. Both are subjected to a point load at the center. Apart from the thickness, the two structures are identical. The panel to which Fig. 7(a) refers is twice as thick as the one to which Fig. 7(b) is related.

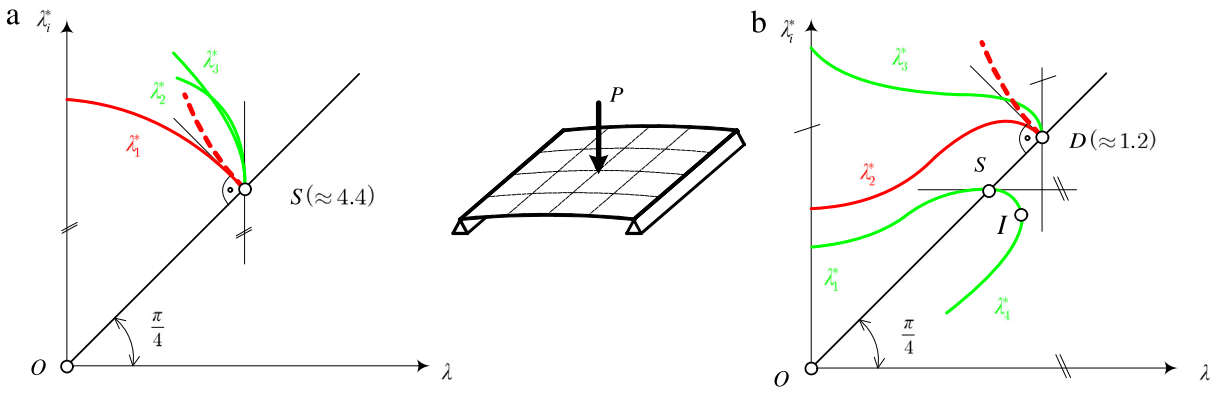

Fig. 7. λ_i^*–λ diagrams for two shallow cylindrical panels of different thickness, with loss of stability by (a) snap-through and (b) bifurcation buckling [1]. (For interpretation of the references to color in this figure legend, the reader is referred to the web version of this article.)

The red curves in Fig. 7 represent "snap-through modes" whereas the green curves show "bifurcation modes". The latter are characterized by [1]

$$\alpha_k^* = \arcsin \frac{\mathbf{v}_k^* \cdot \overline{\mathbf{P}}}{\|\mathbf{v}_k^*\| \, \|\overline{\mathbf{P}}\|} \leq 0.2, \quad (0.2^\circ < \alpha_k^* < 1.0^\circ \text{ uncertainty domain}), \tag{50}$$

where $\overline{\mathbf{P}}$ denotes the vector of node forces, in the framework of the FEM, that are work-equivalent to the reference load.

$\overset{\cdot\cdot}{\widetilde{\mathbf{K}}}_T(\lambda)$ is a real symmetric matrix. In the prebuckling region, $\widetilde{\mathbf{K}}_T(\lambda)$ is a positive definite matrix. Hence, in this region all eigenvalues of the CLE are real. The sign of the reference load can be chosen such that $\lambda_1^* - \lambda > 0$ in the prebuckling region, as is the case in this work. However, it must be borne in mind that there are problems with both a positive and a negative stability limit. One example of such problems is a pressure vessel with a torispherical head, which may buckle under external as well as under internal pressure.

A discussion of Fig. 7 requires knowledge of the value of $\dot{\lambda}_1^*(\lambda_S)$. To determine this value, Eq. (35) is derived with respect to λ, which gives

$$[\dot{\lambda}_1^* \overset{\cdot\cdot}{\widetilde{\mathbf{K}}}_T + (\lambda_1^* - \lambda)\overset{\cdot\cdot\cdot}{\widetilde{\mathbf{K}}}_T] \cdot \mathbf{v}_1^* + [\widetilde{\mathbf{K}}_T + (\lambda_1^* - \lambda)\overset{\cdot\cdot}{\widetilde{\mathbf{K}}}_T] \cdot \dot{\mathbf{v}}_1^* = \mathbf{0}. \tag{51}$$

Premultiplication of Eq. (51) by $\mathbf{v}_1^*$ and use of Eq. (35) yields

$$\dot{\lambda}_1^* = -(\lambda_1^* - \lambda)\frac{\mathbf{v}_1^* \cdot \overset{\cdot\cdot}{\widetilde{\mathbf{K}}}_T \cdot \mathbf{v}_1^*}{\mathbf{v}_1^* \cdot \overset{\cdot}{\widetilde{\mathbf{K}}}_T \cdot \mathbf{v}_1^*}. \tag{52}$$

Notwithstanding the type of the stability limit,

$$\lambda_1^*(\lambda_S) - \lambda_S = 0, \tag{53}$$

as follows from Eq. (35). For stability limits in the form of bifurcation points that do not coincide with snap-through points,

$$\mathrm{d}\lambda > 0. \tag{54}$$

Thus,

$$\frac{\mathbf{v}_1^* \cdot \tilde{\tilde{\mathbf{K}}}_T \cdot \mathbf{v}_1^*}{\mathbf{v}_1^* \cdot \tilde{\tilde{\mathbf{K}}}_T \cdot \mathbf{v}_1^*} \tag{55}$$

is a finite quantity. Therefore, substitution of Eq. (53) into Eq. (52) results in

$$\boxed{\dot{\lambda}_1^*(\lambda_S) = 0}. \tag{56}$$

Snap-through points are characterized by

$$\mathrm{d}\lambda = 0. \tag{57}$$

This suggests a change of the parametrization from λ to ξ. The parameter ξ is defined as

$$\xi = \int \sqrt{\mathrm{d}\mathbf{q} \cdot \mathrm{d}\mathbf{q}}, \tag{58}$$

where $d\mathbf{q}$ is a differential of the vector of nodal displacements, $\mathbf{q}$, in the framework of the FEM. Thus,

$$\mathrm{d}\xi = \sqrt{\mathrm{d}\mathbf{q} \cdot \mathrm{d}\mathbf{q}}, \tag{59}$$

representing a differential arc length. Use of the parameter ξ in the expression on the right-hand side of Eq. (52) gives

$$\dot{\lambda}_1^* = -(\lambda_1^* - \lambda) \frac{\frac{\mathbf{v}_1^* \cdot \left[\widetilde{\mathbf{K}}_{T,\xi\xi}\lambda_{,\xi} - \widetilde{\mathbf{K}}_{T,\xi}\lambda_{,\xi\xi}\right] \cdot \mathbf{v}_1^*}{(\lambda_{,\xi})^3}}{\mathbf{v}_1^* \cdot \frac{\widetilde{\mathbf{K}}_{T,\xi}}{\lambda_{,\xi}} \cdot \mathbf{v}_1^*} = -\frac{\lambda_1^* - \lambda}{(\lambda_{,\xi})^2} \frac{\mathbf{v}_1^* \cdot \left[\widetilde{\mathbf{K}}_{T,\xi\xi}\lambda_{,\xi} - \widetilde{\mathbf{K}}_{T,\xi}\lambda_{,\xi\xi}\right] \cdot \mathbf{v}_1^*}{\mathbf{v}_1^* \cdot \widetilde{\mathbf{K}}_{T,\xi} \cdot \mathbf{v}_1^*}. \tag{60}$$

Specialization of Eq. (60) for a snap-through point, characterized by $\lambda_{,\xi} = 0$, and use of *de L'Hospital's* rule yields

$$\dot{\lambda}_1^* = \frac{\lambda_1^* - \lambda}{(\lambda_{,\xi})^2}\lambda_{,\xi\xi} = \frac{0}{0}\lambda_{,\xi\xi} = \frac{\lambda_{1,\xi}^* - \lambda_{,\xi}}{2\lambda_{,\xi}\lambda_{,\xi\xi}}\lambda_{,\xi\xi} = \frac{1}{2}\left(\frac{\lambda_{1,\xi}^*}{\lambda_{\xi}} - 1\right) = \frac{1}{2}\left(\dot{\lambda}_1^* - 1\right), \tag{61}$$

resulting in

$$\boxed{\dot{\lambda}_1^* = \frac{\lambda_{1,\xi}^*}{\lambda_{,\xi}} = \frac{0}{0} = \frac{\lambda_{1,\xi\xi}^*}{\lambda_{,\xi\xi}} = -1}. \tag{62}$$

Thus, the snap-through point represents a singular point of the curve $\lambda_1^*(\lambda)$ in the form of a cusp.

Fig. 7(a) shows the diagrams $\lambda_i^* - \lambda$, $i = 1, 2, 3$, referring to the thicker shell. The stability limit S is a snap-through point. At this point,

$$\lambda_i^* - \lambda = 0, \tag{63}$$

representing an N-fold null eigenvalue of the CLE. At point S,

$$\dot{\lambda}_1^* = -1, \qquad \dot{\lambda}_2^* = -\infty, \qquad \dot{\lambda}_3^* = -\infty. \tag{64}$$

Consideration of $\lambda_{,\xi} = 0$ in these relations gives

$$\lambda_{1,\xi}^* = 0, \qquad \lambda_{2,\xi}^* < 0, \qquad \lambda_{3,\xi}^* < 0. \tag{65}$$

Consequently, it is the vanishing of $\lambda^*_{1,\xi}$ at the snap-through point that distinguishes the eigenvalue $\lambda^*_1 - \lambda$ from the eigenvalues $\lambda^*_2 - \lambda$ and $\lambda^*_3 - \lambda$ and thus, obviously, from all of the remaining $N - 1$ eigenvalues. This justifies the designation of $\lambda^*_1 - \lambda$ as the fundamental eigenvalue of the CLE.

Fig. 7(b) shows the diagrams $\lambda^*_i - \lambda$, $i = 1, 2, 3, 4$, referring to the thinner shell. The stability limit S is a bifurcation point. At this point,

$$\lambda^*_1 - \lambda = 0, \qquad \dot{\lambda}^*_1 = 0. \tag{66}$$

Because of $\lambda_{,\xi} \neq 0$,

$$\lambda^*_{1,\xi} = 0. \tag{67}$$

At the snap-through point D,

$$\lambda^*_2 - \lambda = 0, \qquad \lambda^*_3 - \lambda = 0 \tag{68}$$

and

$$\dot{\lambda}^*_2 = -1, \qquad \dot{\lambda}^*_3 = -\infty. \tag{69}$$

Consideration of $\lambda_{,\xi} = 0$ in the relations for $\dot{\lambda}^*_2$ and $\dot{\lambda}^*_3$ gives

$$\lambda^*_{2,\xi} = 0, \qquad \lambda^*_{3,\xi} < 0. \tag{70}$$

At point I, with $\lambda_S < \lambda_I < \lambda_D$,

$$\lambda^*_1 = \lambda^*_4. \tag{71}$$

For $\lambda > \lambda_I$, the eigenvalues $\lambda^*_1 - \lambda$ and $\lambda^*_4 - \lambda$ are conjugate complex quantities, noting that for $\lambda > \lambda_S$ $\widetilde{\mathbf{K}}_T(\lambda)$ is an indefinite matrix, which renders conjugate complex eigenvalues possible. Thus, it is the vanishing of $\lambda^*_{1,\xi}$ at the bifurcation point and of $\lambda^*_{2,\xi}$ at the snap-through point, which distinguishes these two eigenvalues from the remaining $N-2$ eigenvalues. However, because of the irrelevance of the snap-through point as compared to the bifurcation point which represents the stability limit, the designation fundamental eigenvalue of the CLE remains restricted to $\lambda^*_1 - \lambda$.

9. Numerical investigation

9.1. Buckling from a membrane stress state

Fig. 8 illustrates a two-hinged arch, subjected to a vertical, uniformly distributed load. The geometric form of the axis of the arch is the one of a parabola, given as

$$x \in [0, L], \quad y = \frac{4H}{L^2} x(L - x). \tag{72}$$

The cross-section is constant. Its form is rectangular. The values of the geometric and the cross-sectional parameters, L, H and A, I, respectively, of the modulus of elasticity, E, and of the reference load, $\bar{p}$, are also shown in Fig. 8. Contrary to a three-hinged arch of the same geometric configuration, subjected to the same load as the two-hinged arch shown in Fig. 8, the latter is actually no thrust-line arch. However, since the bending moments are negligibly small, it is justified to consider it approximately as such an arch. For a thrust-line arch, buckling occurs from a membrane stress state.

The structure was analyzed by the commercial FE software MSC.MARC (element #52 [12]) and by the program FEM_{v2}, which was written by the third author of this work [13]. It is characterized by the analytical determination of $\widetilde{\mathbf{K}}_T$ and $\check{\mathbf{K}}_T$ for a co-rotational finite beam element, based on the Euler–Bernoulli assumptions, see Appendix B.1.2. Details of the numerical solution of the CLE are presented in Appendices B and C. The arch was discretized by 100 two-node beam elements. The displacement of the apex, u, was chosen as the representative degree of freedom. A positive value of u indicates a displacement in the direction of the load. The λ–u diagrams, obtained from FE_{v2} and MSC.MARC, respectively, are shown in Fig. 9(a). They contain the bifurcation point $S = B$, followed by the snap-through point D. Hence, the latter is physically insignificant. The result obtained from MSC.MARC agrees very well

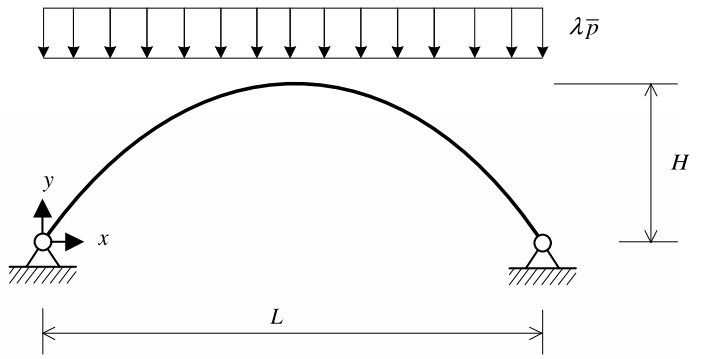

Fig. 8. Configuration, material properties, and load of a two-hinged parabolic arch.

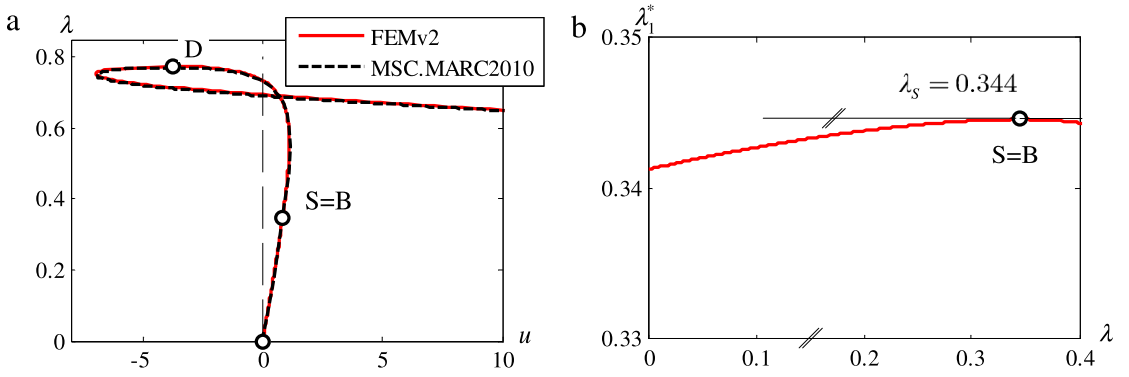

Fig. 9. (a) λ–u diagrams and (b) λ_1^*–λ diagram of a two-hinged parabolic arch, subjected to a vertical, uniformly distributed load.

with the one obtained from FE_{v2}. Fig. 9(b) illustrates the λ_1^*–λ diagram. Its nonlinearity, though very small in the given case, is a characteristic feature of a nonlinear stability problem. At the bifurcation point, $\lambda_1^* = \lambda_S$, see Eq. (53), and $\dot{\lambda}_1^* = 0$, see Eq. (56).

Fig. 10 shows $(\mathbf{v}_{10}^* \cdot \mathbf{v}_1^*)$–λ diagrams, where $\mathbf{v}_{10}^* = \mathbf{v}_1^*(0)$, see Eq. (3). The impression of a straight horizontal line in Fig. 10(a) allows the conclusion that for a genuine thrust-line arch $\mathbf{v}_1^*$ would be constant in the prebuckling regime, which confirms the presentation in Section 6, see Fig. 6. Incidentally, stability analysis of a *von Mises truss*, which is not documented in this work, has also confirmed this presentation. This example is characterized by a significantly stronger nonlinearity of the λ_1^*–λ diagram than the one of the two-hinged parabolic arch, subjected to a vertical, uniformly distributed load. The constancy of $\mathbf{v}_1^*$ implies satisfaction of specific *physical orthogonality conditions*, see Eq. (38) and Table 1, and, furthermore, of the hypothesis for $(U - U_M)/U$, see Eq. (41). As a counterpoint, Fig. 10(b) illustrates a $(\mathbf{v}_{10}^* \cdot \mathbf{v}_1^*)$–λ diagram for a two-hinged circular arch, subjected to a vertical point load at the apex [14]. Since this arch also experiences bending deformations in the prebuckling regime, $\mathbf{v}_{10}^* \cdot \mathbf{v}_1^*$ is variable, becoming a minimum at the bifurcation point $S = B$. This follows from specialization of Eq. (36) for the bifurcation point, i.e. for $\lambda_1^*(\lambda_S) - \lambda_S = 0$, see Eq. (53). Noting that

$$\frac{\mathbf{v}_j^* \cdot \tilde{\tilde{\mathbf{K}}}_T \cdot \mathbf{v}_1^*}{(\lambda_1^* - \lambda_j^*)\, \mathbf{v}_j^* \cdot \tilde{\tilde{\mathbf{K}}}_T \cdot \mathbf{v}_j^*} \tag{73}$$

remains finite at this point,

$$c_{1j}^*(\lambda_S) = 0. \tag{74}$$

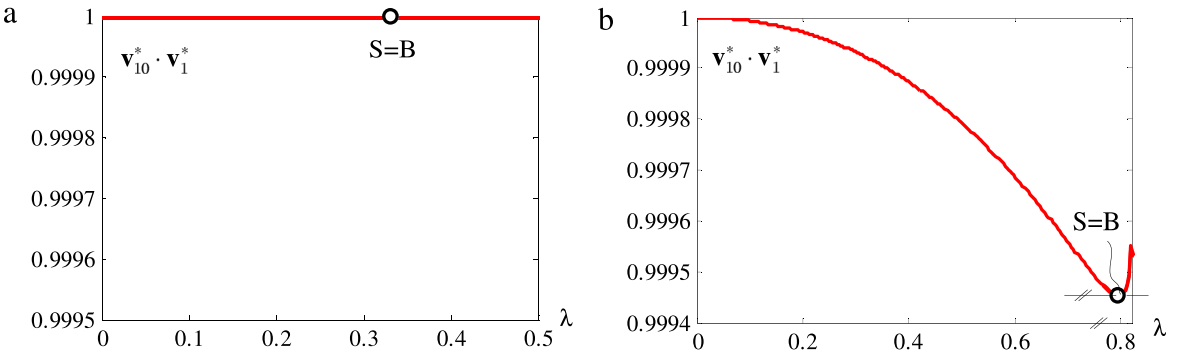

Fig. 10. $(\mathbf{v}_{10}^{*} \cdot \mathbf{v}_{1}^{*})$–λ diagram of (a) a two-hinged parabolic arch, subjected to a vertical, uniformly distributed load, and (b) a two-hinged circular arch, subjected to a vertical point load at the apex.

Table 1

Approximate satisfaction of the *physical orthogonality conditions* $\mathbf{v}_{j}^{*} \cdot \overset{\circ\circ}{\mathbf{K}}_{T} \cdot \mathbf{v}_{1}^{*} = 0$, $j \neq 1$, e.g. for $j = 2, 3, 4$ at $\lambda = 0$.

	$j = 2$	$j = 3$	$j = 4$
$\mathbf{v}_{j}^{*} \cdot \overset{\circ\circ}{\mathbf{K}}_{T} \cdot \mathbf{v}_{1}^{*}$	7.4952×10^{-5}	-4.1178×10^{-5}	-2.5294×10^{-5}

Substitution of Eq. (74) into Eq. (37) gives

$$\dot{\mathbf{v}}_{1}^{*}(\lambda_S) = \mathbf{0}, \tag{75}$$

defining a singular point of the fictitious curve on the surface of the unit sphere, described by the vertex of the vector $\mathbf{v}_{1}^{*}(\lambda)$ [11]. Thus, following from Eq. (2),

$$\frac{\mathrm{d}}{\mathrm{d}\lambda}(\cos\,\varphi) = -\dot{\varphi}\sin\varphi = \frac{\mathrm{d}}{\mathrm{d}\lambda}(\mathbf{v}_{10}^{*} \cdot \mathbf{v}_{1}^{*}) = \mathbf{v}_{10}^{*} \cdot \dot{\mathbf{v}}_{1}^{*} = 0, \tag{76}$$

indicating an extreme value of the functions $\varphi(\lambda)$ and $\mathbf{v}_{10}^{*} \cdot \mathbf{v}_{1}^{*}(\lambda)$. $\varphi(\lambda_S)$ is a maximum, whereas $\mathbf{v}_{10}^{*} \cdot \mathbf{v}_{1}^{*}(\lambda_S)$ is a minimum, see Fig. 10(b).

9.2. *Buckling from a pure bending stress state*

Fig. 11 illustrates a fork-supported beam, subjected to bending moments $\lambda\,\overline{M_y}$ about the horizontal axis y at both ends. The cross-section of the beam is the one of an IPE-400. The values of the length of the beam, L, the cross-sectional parameters A, I_y, I_z, I_t, I_ω, the elastic constants, E, ν, and of the reference bending moment, $\overline{M_y}$, are also shown in Fig. 11. I_t denotes the torque of inertia about the longitudinal axis x and I_ω stands for the warping constant.

For the numerical investigation of lateral buckling of the beam 1200 bilinear shell elements (element #75 [12]) were used. This discretization is based on a preliminary convergence study. Fig. 12 shows the first three eigenmodes.

FE stability analysis by means of MSC.MARC resulted in

$$\lambda_S = 0.531 \tag{77}$$

as the value of the load parameter at the stability limit. It differs little from

$$\lambda_S = 0.526, \tag{78}$$

representing the result from an analytical solution [15], based on

$$M_{cr,y} = \lambda\,\overline{M_y} = N_{Ki,z} \cdot c, \tag{79}$$

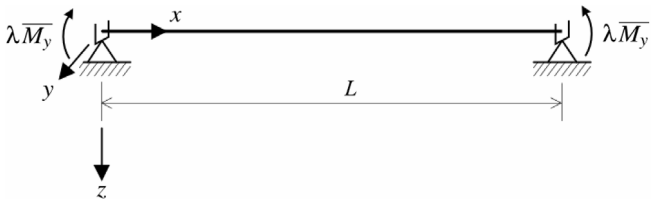

$\overline{M}_y = 50\,000\,kN cm \qquad I_y = 21876.5\,cm^4 \qquad E = 20000\,kN/cm^2$
$A = 84.5\,cm^2 \qquad I_z = 1314.18\,cm^4 \qquad \nu = 0.3$
$L = 500\,cm \qquad I_t = 36.32\,cm^4$
$I_\omega = 490000\,cm^6$

Fig. 11. Configuration, material properties, and bending moment of a fork-supported IPE-400.

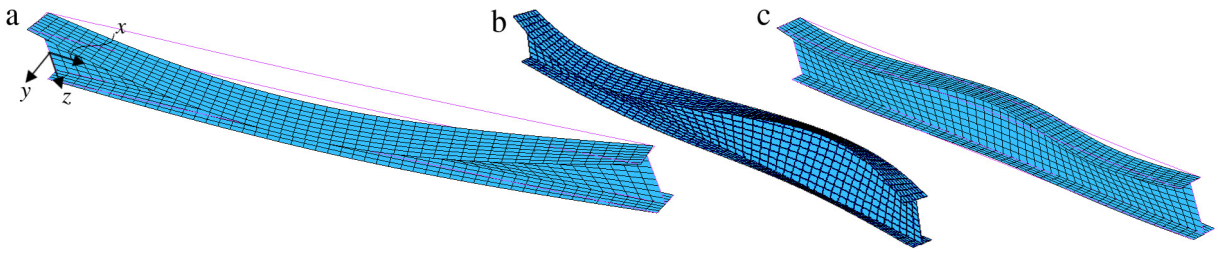

Fig. 12. Lateral buckling of the beam shown in Fig. 11: (a) first, (b) second, (c) third eigenmodes.

Table 2
Fork-supported IPE-400, subjected to bending moments about the horizontal axis y at both ends: Approximate satisfaction of the condition $(U - U_M)/U = 1$.

	λ/λ_S						
	0.20	0.40	0.60	0.80	0.90	0.95	0.975
$\frac{U-U_M}{U}$	1.00194	1.00045	0.99953	1.00000	1.00106	1.00146	1.00038

where

$$N_{Ki,z} = \frac{\pi^2 \cdot E I_z}{L^2}, \qquad c = \sqrt{\frac{I_\omega + 0.039 \cdot L^2 \cdot I_t}{I_z}}. \tag{80}$$

Small differences concerning the realization of the boundary conditions may be the reason for the small difference between the two values of λ_S.

Fig. 13(a) shows the λ_1^*–λ diagram. Fig. 13(b) illustrates the $(\mathbf{v}_{10}^* \cdot \mathbf{v}_1^*)$–$\lambda$ diagram. The variability of $\mathbf{v}_{10}^* \cdot \mathbf{v}_1^*$ is the consequence of bending in the prebuckling regime. Analogous to the situation for the circular arch subjected to a point load at the apex (see Fig. 10(b)), $\mathbf{v}_{10}^* \cdot \mathbf{v}_1^*$ becomes a minimum at the bifurcation point S. Following from Fig. 13(b), $\varphi(\lambda_S) = \arccos(\mathbf{v}_{10}^* \cdot \mathbf{v}_1^*(\lambda_S))$ is very small.

Fig. 14(a) shows the ρ–λ diagram. The singularity $\rho(\lambda_S) = 0$, see Eq. (A.15.2), prevents the function $\rho(\lambda) = -\mathbf{v}_1^* \cdot \mathbf{n}$, see Eq. (42), from fulfilling the originally anticipated condition $\rho(\lambda) = 1$, which was later found to be outside the region of validity of $\rho(\lambda)$, see Eq. (49). Nevertheless, the deviation of $\rho(\lambda)$ from 1 increases from 0.9% for $\lambda/\lambda_S = 0.10$ to only 2.8% for $\lambda/\lambda_S = 0.975$. Fig. 14(b) contains the c–λ diagram. Although the condition $c(\lambda) = 1$, see Eq. (48), is not satisfied, the quality of the approximation of $(U - U_M)/U = 1$ is excellent, see Table 2. This is the consequence of the small deviation of $\rho(\lambda)$ from 1, with the exception of the immediate vicinity of the stability limit.

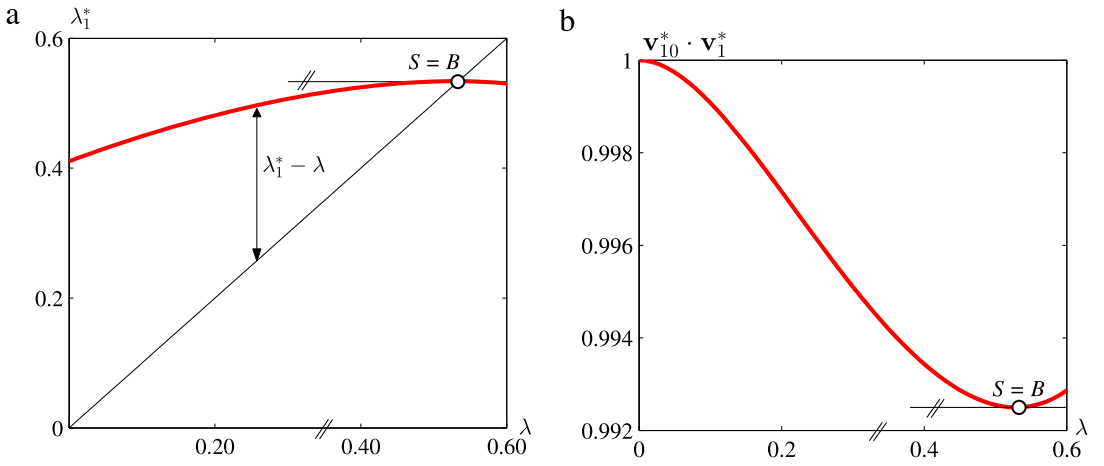

Fig. 13. Fork-supported IPE-400, subjected to bending moments about the horizontal axis y at both ends: (a) λ_1^*–λ diagram, (b) $(\mathbf{v}_{10}^* \cdot \mathbf{v}_1^*)$–$\lambda$ diagram.

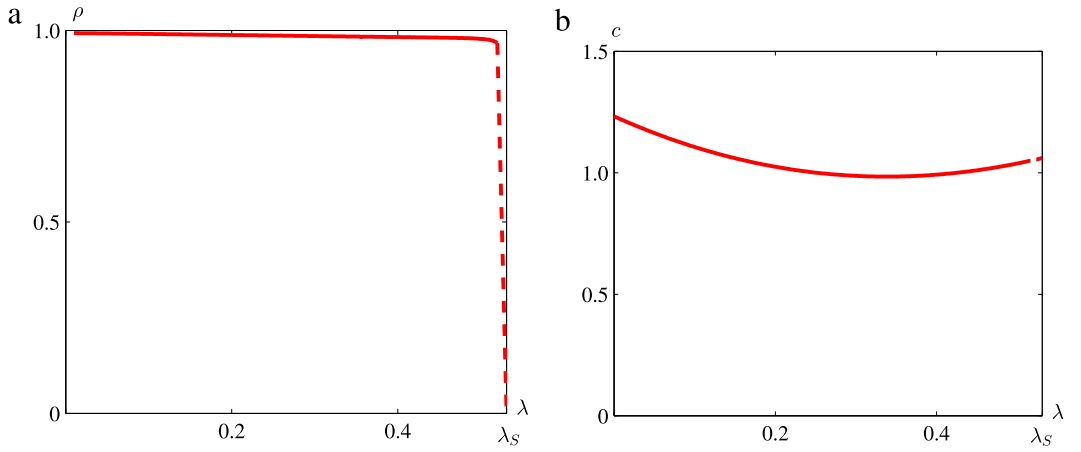

Fig. 14. Fork-supported IPE-400, subjected to bending moments about the horizontal axis y at both ends: (a) ρ–λ diagram, (b) c–λ diagram.

For a pure bending stress state in the prebuckling regime,

$$\mathbf{a}(\theta(\lambda), \varphi(\lambda)) = \begin{Bmatrix} \cos\varphi \\ \sin\varphi \\ 0 \end{Bmatrix}, \tag{81}$$

see Fig. 15. As follows from Fig. 13(b),

$$\varphi(\lambda_S) = \arccos\left(\mathbf{v}_{10}^* \cdot \mathbf{v}_1^*(\lambda_S)\right) \tag{82}$$

is very small. In the given case, $\varphi(\lambda_S)$ is equal to the angle enclosed by $\mathbf{e}_x$ and $\mathbf{a}(\lambda_S)$. To avoid the impression of a constant vector $\mathbf{a}(\lambda) = \mathbf{e}_x$, the deviation of $\mathbf{a}(\lambda_S)$ from $\mathbf{e}_x$ was very strongly magnified in Fig. 15. The angle $\varphi(\lambda_S)$ is assumed to correlate with an expression that depends on both the "non-membrane" deformations and the stiffness of the structure at incipient buckling. The hypothesis concerned reads as follows:

$$\tan\varphi(\lambda_S) = \left(\xi(\lambda_S) - \xi_M(\lambda_S)\right)\left|1 - \frac{\lambda_{,\xi}(\lambda_S)}{\lambda_{,\xi}(0)}\right|, \quad 0 \le \varphi(\lambda_S) \le \frac{\pi}{2}, \tag{83}$$

with ξ according to Eq. (58) and ξ_M as its membrane part. For the limiting case of a pure bending stress state,

$$\xi_M(\lambda_S) = 0, \tag{84}$$

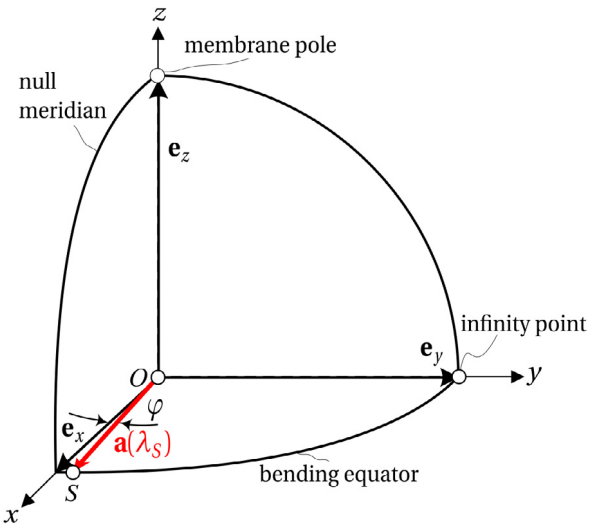

Fig. 15. Pure bending stress state.

resulting in

$$\tan\,\varphi(\lambda_S) = \xi(\lambda_S)\left|1 - \lambda_{,\xi}(\lambda_S)\right|, \tag{85}$$

if the reference load is chosen such that $\lambda_{,\xi}(0) = 1$.

Because of the very small deviations of the prebuckling paths of the given problem from linearity,

$$0 < \xi(\lambda_S)\left|1 - \lambda_{,\xi}(\lambda_S)\right| \ll 1. \tag{86}$$

This was borne in mind when comparing the extremely small angle $\varphi(\lambda_S)$ in the present example, characterized by $U_M(\lambda) = 0$, with $\varphi(\lambda_S) = \pi/2$ in Fig. 4, characterized by $U_M/U|_{\lambda=\lambda_S} = 0$, where, however, $U_M(\lambda_S) \neq 0$, $U(\lambda_S) = \infty$. For that problem,

$$\xi(\lambda_S) = \infty, \qquad \xi_M(\lambda_S) \neq \infty, \qquad \lambda_{,\xi}(\lambda_S) = 0, \tag{87}$$

resulting in

$$\tan\varphi(\lambda_S) = \infty \implies \varphi(\lambda_S) = \frac{\pi}{2}, \tag{88}$$

see Fig. 5(c).

Contrary to the very small angle $\varphi(\lambda_S)$ for the fork-supported IPE-400, subjected to pure bending, the variability of $\rho(\lambda)$ shortly before the stability limit is great, see Fig. 14(a). Thus, $\mathbf{n}(\lambda)$, appearing in the formula for $\rho(\lambda)$, see Eq. (42), may vary strongly even if $\mathbf{v}_1^*(\lambda)$ varies only very little.

The numerical investigation of the limiting case of a pure bending stress state permits the conclusion that the hypothesis for $(U - U_M)/U$, see Eq. (41), is useful for the special case of $(U - U_M)/U = const.$ For the limiting case concerned, the maximum deviation from the desired value 1 is less than 1% in the range of $0.20 \leq \lambda/\lambda_S \leq 0.975$, see Table 2. For the limiting case of a membrane stress state, the exact solution is obtained, apart from negligibly small numerical errors.

9.3. Buckling from a general stress state

9.3.1. Angular measurement

The angle ψ, which is enclosed by d$\mathbf{a}$ $(\theta(\lambda), \varphi(\lambda))$ and the coordinate line $\theta = const.$, is obtained from

$$\tan\,\psi = \frac{1}{\sin\,\theta}\frac{\mathrm{d}\theta}{\mathrm{d}\varphi}, \tag{89}$$

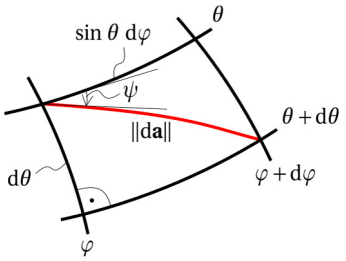

Fig. 16. On determination of the angle ψ.

see Fig. 16. $\mathrm{d}\theta$ follows from Eq. (2) as

$$\mathrm{d}\theta = -\frac{1}{\sin\,2\theta}\,\mathrm{d}\left(\frac{U_M}{U}\right) \tag{90}$$

and $\mathrm{d}\varphi$ from Eq. (3) as

$$\mathrm{d}\varphi = -\frac{1}{\sin\,\varphi}\mathbf{v}_{10}^{*}\cdot\mathrm{d}\mathbf{v}_{1}^{*}. \tag{91}$$

Substitution of Eqs. (90) and (91) into Eq. (89) gives

$$\tan\,\psi = \frac{\sin\,\varphi}{\sin\,\theta\,\sin\,2\theta}\,\frac{\mathrm{d}\left(\frac{U_M}{U}\right)}{\mathbf{v}_{10}^{*}\cdot\mathrm{d}\mathbf{v}_{1}^{*}}. \tag{92}$$

The angle ψ is visualized on the buckling sphere in Fig. 28.

At the stability limit,

$$\mathrm{d}\mathbf{v}_{1}^{*}(\lambda_S) = \mathbf{0}. \tag{93}$$

This result follows from Eq. (75), which was obtained for a stability limit in the form of a bifurcation point. It must obviously also hold for a stability limit in the form of a snap-through point. To show this, the parametrization in the expression for c_{1j}^{*}, see Eq. (36), is changed from λ to ξ. This results in

$$c_{1j}^{*} = -\frac{\lambda_1^{*}-\lambda}{\lambda_1^{*}-\lambda_j^{*}}\,\frac{\mathbf{v}_j^{*}\cdot\frac{\widetilde{\mathbf{K}}_{T,\xi\xi}\lambda_{,\xi}-\widetilde{\mathbf{K}}_{T,\xi}\lambda_{,\xi\xi}}{(\lambda_{,\xi})^3}\cdot\mathbf{v}_1^{*}}{(\lambda_1^{*}-\lambda_j^{*})\mathbf{v}_j^{*}\cdot\frac{\widetilde{\mathbf{K}}_{T,\xi}}{\lambda_{,\xi}}\cdot\mathbf{v}_j^{*}} = -\frac{\lambda_1^{*}-\lambda}{\lambda_1^{*}-\lambda_j^{*}}\,\frac{\mathbf{v}_j^{*}\cdot\frac{\widetilde{\mathbf{K}}_{T,\xi\xi}}{\lambda_{,\xi}}\cdot\mathbf{v}_1^{*}}{\mathbf{v}_j^{*}\cdot\widetilde{\mathbf{K}}_{T,\xi}\cdot\mathbf{v}_j^{*}}, \tag{94}$$

where use of the orthogonality relation

$$\mathbf{v}_j^{*}\cdot\widetilde{\mathbf{K}}_{T,\xi}\cdot\mathbf{v}_1^{*} = 0, \tag{95}$$

following from Eq. (39.2), was made. Substitution of Eq. (94) into

$$\dot{\mathbf{v}}_1^{*} = \frac{\mathbf{v}_{1,\xi}^{*}}{\lambda_{,\xi}} = \sum_{j=2}^{N} c_{1j}^{*}\cdot\mathbf{v}_j^{*} \tag{96}$$

gives

$$\mathrm{d}\mathbf{v}_1^{*} = -(\lambda_1^{*}-\lambda)\left(\sum_{j=2}^{N}\frac{\mathbf{v}_j^{*}\cdot\widetilde{\mathbf{K}}_{T,\xi\xi}\cdot\mathbf{v}_1^{*}}{(\lambda_1^{*}-\lambda_j^{*})\mathbf{v}_j^{*}\cdot\widetilde{\mathbf{K}}_{T,\xi}\cdot\mathbf{v}_j^{*}}\mathbf{v}_j^{*}\right)\mathrm{d}\xi. \tag{97}$$

Recalling that the snap-through point corresponds to an N-fold eigenvalue of the CLE, see Section 8,

$$\lambda_1^{*}(\lambda_S)-\lambda_S = 0, \qquad \lambda_1^{*}(\lambda_S)-\lambda_j^{*}(\lambda_S) = 0, \quad j = 2,3,\ldots,N. \tag{98}$$

Application of *de L'Hospital's* rule and use of the relations (65) and of Eq. (67) yields

$$\frac{\lambda_1^* - \lambda}{\lambda_1^* - \lambda_j^*}\Big|_{\lambda=\lambda_S} = \frac{0}{0} = \frac{\lambda_{1,\xi}^* - \lambda_{,\xi}}{\lambda_{1,\xi}^* - \lambda_{j,\xi}}\Big|_{\lambda=\lambda_S} = \frac{0-0}{0-\lambda_{j,\xi}^*} = 0. \tag{99}$$

Substitution of Eq. (99) into Eq. (97) confirms Eq. (93). Insertion of this relation into Eq. (92) gives

$$|\tan\ \psi(\lambda_S)| = \infty, \tag{100}$$

see the meridional tangent to the surface curve in Fig. 2.

9.3.2. Snap-through of a circular arch

Fig. 17 illustrates a circular arch, subjected to a vertical point load at the apex. Its left end is fixed and its right end is simply supported. The cross-section is constant. Its form is rectangular. The values of the radius R, the included angle μ, the bending stiffness EI, the axial stiffness EA, the shear stiffness $GA/\varkappa$, where G is the shear modulus and $\varkappa$ is the shear correction factor, and of the reference load $\overline{P}$ are also shown in Fig. 17. The shear stiffness is obtained by dividing the axial stiffness by $2(1+\nu)\varkappa$, assuming $\nu = 0.25$ and considering $\varkappa = 1.2$.

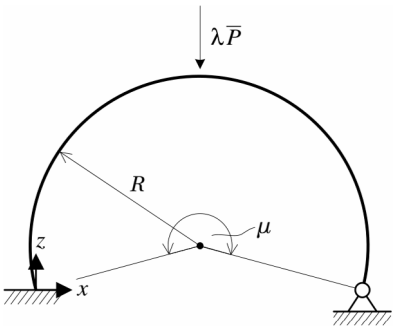

$R = 1907.4\,cm$ $\quad \mu = 215°$ $\quad \overline{P} = 1000\,kN$

$EI = 10^8\,kNcm^2$ $\quad EA = 5 \cdot 10^4\,kN$ $\quad GA/\varkappa = 16666.7\,kN$

Fig. 17. Configuration, stiffnesses, and load of a circular arch, fixed at one end and simply supported at the other one.

The arch was analyzed by MSC.MARC (element #98 [12]) for three different FE discretizations (100, 200, 400 elements). Fig. 18(a) shows λ–w diagrams, where w denotes the vertical component of the displacement of the apex. The positive values of w indicate displacement components in the direction of the load. Fig. 18(b) illustrates λ–φ diagrams, where φ stands for the rotation of the apex. A positive value of φ indicates a counterclockwise rotation. At the stability limit S, $\mathrm{d}\lambda = 0$. Thus, loss of stability occurs by snap-through. The results obtained by the three FE discretizations differ very little. This is reflected by the very small distances between the respective stability limits, see the details in Fig. 18(a) and (b). The ordinates λ_S of these points are less than 4% larger than the value of λ_S, reported in [1]. Fig. 18(a) shows that the λ–w diagram is strongly nonlinear and that the displacement at the stability limit is very large. Fig. 18(b) illustrates that $\varphi(\lambda)$ has a maximum in the prebuckling regime. In the following, the FE discretization with 200 elements is used.

Fig. 19(a) shows the fundamental eigenform for $\lambda = 0$, representing part of the result of an initial eigenvalue analysis by means of the CLE. It corresponds to the one depicted in [1]. Fig. 19(b) illustrates the deformed arch for $\lambda = 0.84$, i.e. just before reaching the stability limit $\lambda_S = 0.85$, and the fundamental eigenform for this value of λ, based on the CLE. Both curves agree well with corresponding curves shown in [1].

Fig. 20(a) shows the λ_1^*–λ diagram. At the snap-through point D, representing the stability limit, i.e. $S = D$, $\dot{\lambda}_1^* = -1$, see Eq. (62). (The resolution in Fig. 20(a) is not fine enough to show the maximum of $\lambda_1^*(\lambda)$ just before the stability limit.) The form of the diagram is typical for a pronounced nonlinearity of the prebuckling region, combined with large deformations at the stability limit. Fig. 20(b) illustrates the $(\mathbf{v}_{10}^* \cdot \mathbf{v}_1^*)$–$\lambda$ diagram. At the stability limit,

$$\frac{\mathrm{d}}{\mathrm{d}\lambda}(\cos\ \varphi) = -\dot{\varphi}\sin\varphi = \frac{\mathrm{d}}{\mathrm{d}\lambda}(\mathbf{v}_{10}^* \cdot \mathbf{v}_1^*) = \mathbf{v}_{10}^* \cdot \dot{\mathbf{v}}_1^* = \mathbf{v}_{10}^* \cdot \frac{\mathbf{v}_{1,\xi}^*}{\lambda_{,\xi}} = \mathbf{v}_{10}^* \cdot \frac{\mathbf{0}}{0} = \mathbf{v}_{10}^* \cdot \frac{\mathbf{v}_{1,\xi\xi}^*}{\lambda_{,\xi\xi}}, \tag{101}$$

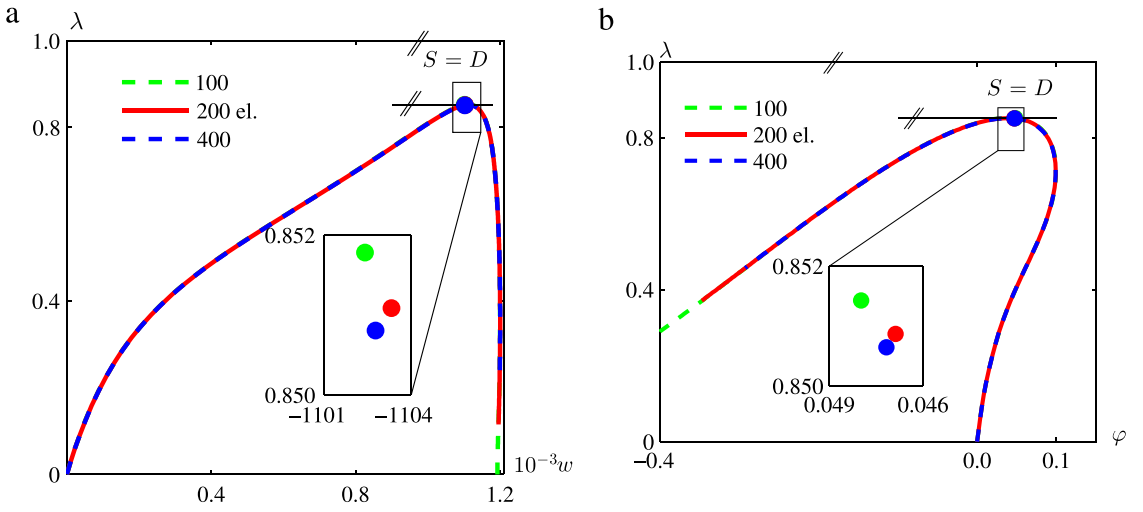

Fig. 18. (a) λ–w diagrams (w in [cm]) and (b) λ–φ diagrams (φ in [rad]) for the apex of the circular arch shown in Fig. 17.

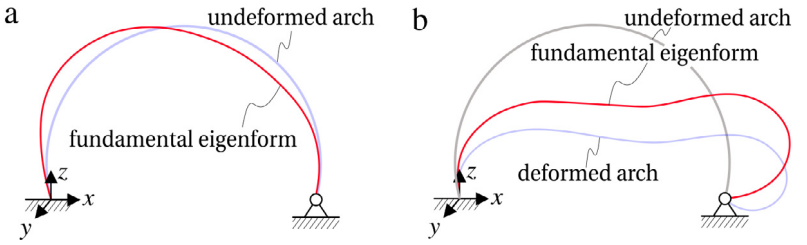

Fig. 19. (a) Fundamental eigenform for λ = 0, (b) deformed arch at λ = 0.84 (without superelevation) and corresponding eigenform.

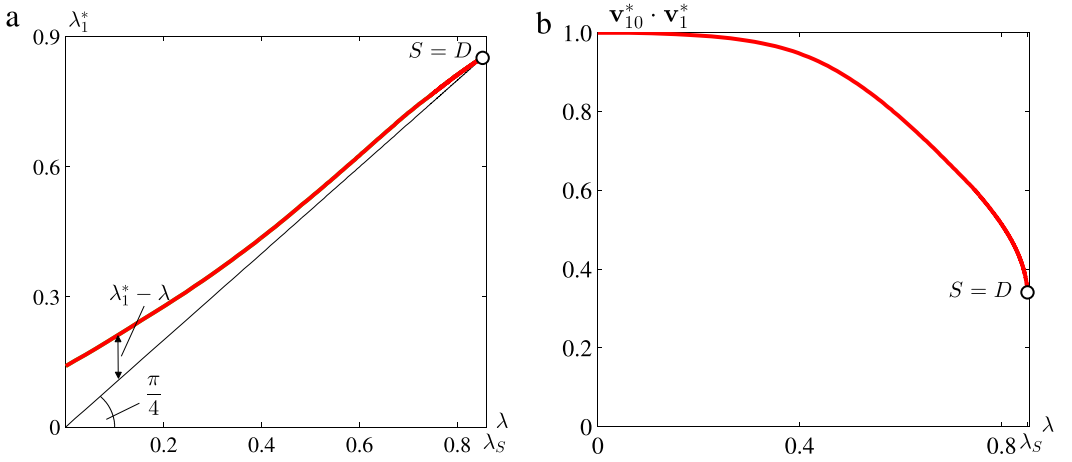

Fig. 20. (a) λ_1^*–λ diagram and (b) $(\mathbf{v}_{10}^* \cdot \mathbf{v}_1^*)$–λ diagram for the circular arch shown in Fig. 17.

where use of Eq. (57), Eq. (93), and of *de L'Hospital's* rule was made. Thus, analogous to the curve $\lambda_1^*(\lambda)$, the snap-through point represents a singular point of the curve $\mathbf{v}_{10}^* \cdot \mathbf{v}_1^*(\lambda)$ in the form of a cusp. The cusps do not appear in Fig. 20, because the two curves were only plotted up to the stability limit.

Fig. 21 illustrates the curve $\mathbf{a}\,(\theta(\lambda), \varphi(\lambda))$ on the surface of the buckling sphere for the circular arch shown in Fig. 17. The angle $\theta(\lambda)$ was obtained in a conventional manner, see Appendix B.3. It was also computed by means of the hypothesis for $(U - U_M)/U$, see Eq. (41). However the result did not agree with the one from the conventional analysis. Thus, the hypothesis for the zenith angle could not be verified for the general case. Different from the two

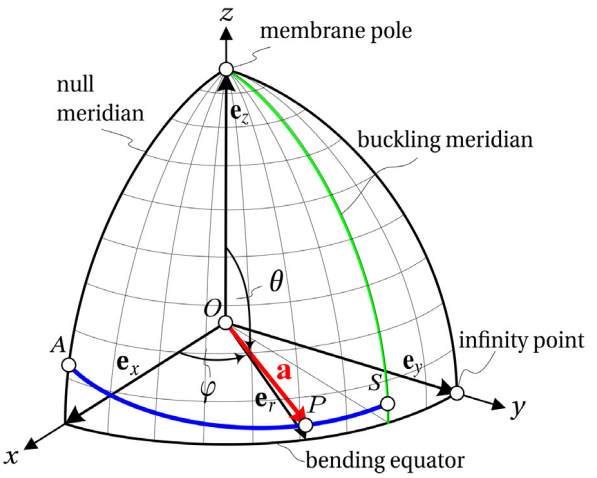

Fig. 21. $\mathbf{a}(\theta(\lambda), \varphi(\lambda))$ for a general stress state, as obtained for the circular arch shown in Fig. 17.

limiting cases, where the fundamental eigenvector is either constant (membrane stress state) or varies only extremely little (pure bending stress state), this is not necessarily the case for a general stress state, see Fig. 20(b). For such a stress state the functions $\rho(\lambda)$ and $c(\lambda)$ are obviously more complicated, which renders superposition in the form of Eq. (41) difficult, if not impossible. However, this is not crucial to the concept of the buckling sphere, because the zenith angle can alternatively and more conveniently be computed in a conventional manner.

The angle θ is large and varies relatively little with φ. Thus, as follows from Eq. (2), $(U - U_M)/U$ is relatively large in the entire prebuckling regime, as compared to its energetical complement U_M/U. Incidentally, the influence of the number of finite elements on these results was found to be negligibly small. This is the logical consequence of the insensitivity of the load–displacement diagrams in Fig. 18 to this number. Fig. 21 also shows that $\theta(\varphi)$ may be a nonmonotonic function. In the present case, at the stability limit,

$$\mathrm{d}\left(\frac{U_M}{U}\right) > 0 \implies \mathrm{d}\theta < 0. \tag{102}$$

Furthermore, for $\lambda = \lambda_S$,

$$\mathrm{d}\mathbf{v}_1^* = \mathbf{0} \implies \mathrm{d}\varphi = 0. \tag{103}$$

Substitution of these relations into Eq. (89) and Eq. (92), respectively, gives

$$\tan\,\psi(\lambda_S) = -\infty. \tag{104}$$

The illustration of the surface curve in Fig. 21 ends at the stability limit. Its large curvature at this point, which cannot be seen in this illustration, may give the wrong impression that the curve is not tangent to the buckling meridian.

A comparison of the result for $\mathbf{a}(\theta(\lambda), \varphi(\lambda))$ for the present problem with the one for the previous problem of buckling from a pure bending stress state shows that the most essential difference between the two surface curves is the angle $\varphi(\lambda_S)$. It is extremely small for the previous problem, but large for the present one. This is the consequence of the fundamental difference between the prebuckling regions of the two problems. It manifests itself in practically linear load–displacement paths with relatively small displacements at the stability limit for the previous problem in contrast to the pronounced nonlinearity of these paths and the extremely large deformations at the stability limit for the present problem. The slight decrease of the zenith angle before the stability limit in this problem, see Fig. 21, is the consequence of the relatively strong membrane tension in the vicinity of the application point of the load.

9.3.3. Bifurcation buckling of a spherical cap

Fig. 22 illustrates one half of a simply supported spherical cap of constant thickness, subjected to a vertical point load at the apex. The values of the radius R, the thickness t, the radius of the base circle, R_0, the rise f, Young's modulus E, Poisson's ratio ν, and of the reference load $\overline{P}$ are also shown in Fig. 22. The fundamental eigenform of

the shell has one symmetry plane. Herein it is chosen as the x–z plane, see Fig. 22. Thus, the analysis is restricted to one half of the shell, characterized by $y \leq 0$.

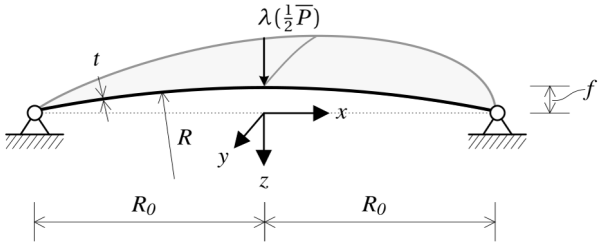

$R = 313.0\,cm$ $t = 0.015\,cm$ $R_0 = 5.0 \cdot 25\,cm$ $f = 1.0\,cm$

$E = 21 \cdot 10^3\,kN cm^2$ $\nu = 0.3$ $\overline{P} = 250\,N$

Fig. 22. Configuration, material parameters, and load of a spherical cap, simply supported along its edge.

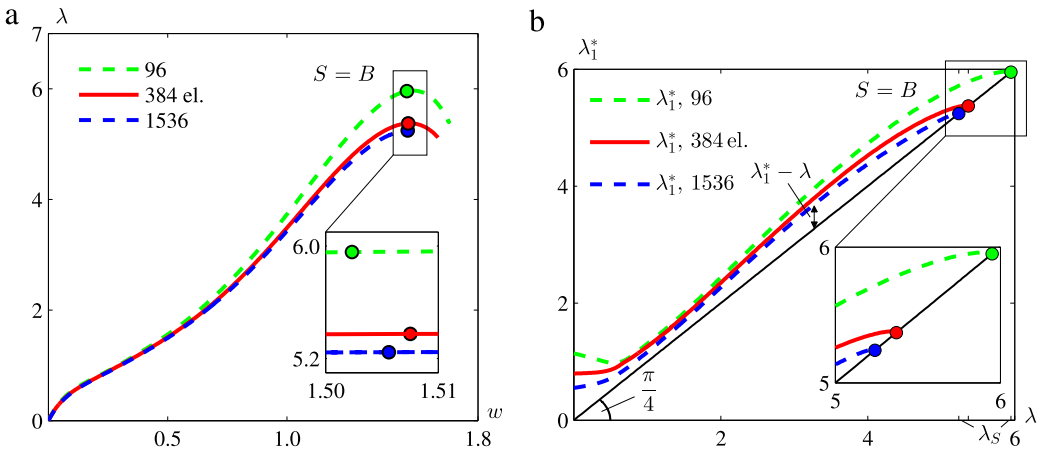

Fig. 23. (a) λ–w diagrams (w in [cm]) for the apex of the spherical cap shown in Fig. 22, (b) λ_1^*–λ diagram for this shell.

The shell was analyzed by MSC.MARC (element #75 [12]) for three different discretizations (96, 384, 1536 elements). Fig. 23(a) shows λ–w diagrams for these discretizations, where w denotes the deflection of the apex. The positive values of w indicate displacements in the direction of the load. The buckling load obtained by means of the middle one mesh is 9.8% smaller than the one computed with the coarsest mesh and the buckling load obtained by the finest mesh is 2.4% smaller than the one computed with the middle one mesh. Fig. 23(a) shows that up to approximately $\lambda = 2$ the three curves agree very well. They reflect the local behavior of the structure at the apex and in its vicinity. It is characterized by initial softening, followed by stiffening due to membrane tension activated by pronounced local bending and, subsequently, by softening until, finally, the stability limit is reached in the form of a bifurcation point immediately before a maximum value of λ. Fig. 23(b) shows the λ_1^*–λ diagrams. Qualitatively, they are similar to the one of the previous example, see Fig. 20(a). Their form is typical for a pronounced nonlinearity in the prebuckling region, combined with large deformations at the stability limit. They contain two points each, at which $\dot{\lambda}_1^* = 1$. The region between these two points is loosely connected with the region between the two points of inflection in the λ–w diagrams in Fig. 23(a), noting that these diagrams just refer to a single degree of freedom. In any case, these intermediate regions are indicators of the variable load-carrying mechanism of the shell in the prebuckling domain.

In the following, the FE discretization with 384 elements is used. Fig. 24(a) shows the fundamental eigenform for $\lambda = 0$, representing part of the result of an initial eigenvalue analysis by means of the CLE. Fig. 24(b) illustrates the eigenform for $\lambda = 5.364$, i.e. just before the stability limit. The plus sign in the color scales refers to displacements in the inward direction of the undeformed shell, and the minus sign to displacements in the outward direction.

Fig. 25 illustrates the $(\mathbf{v}_{10}^* \cdot \mathbf{v}_1^*)$–$\lambda$ diagram. It proves the significant variation of the fundamental eigenform in the prebuckling region, characterized by a steep drop of the function $\mathbf{v}_{10}^* \cdot \mathbf{v}_1^*(\lambda)$ in a relatively small load interval at a comparatively low load level.

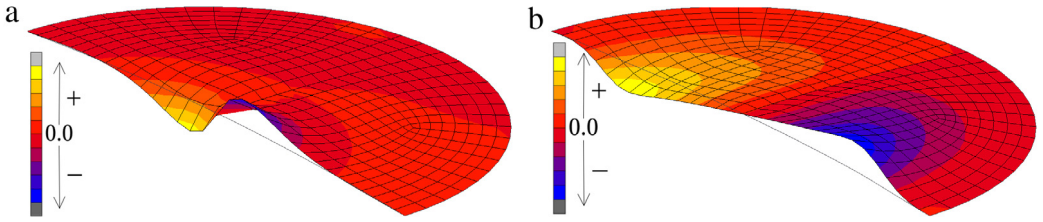

Fig. 24. Fundamental eigenform for (a) $\lambda = 0$ and (b) $\lambda = 5.364$.

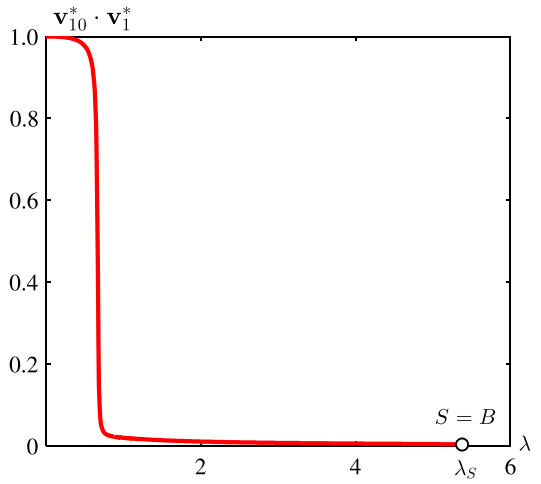

Fig. 25. $(\mathbf{v}_{10}^* \cdot \mathbf{v}_1^*)$-$\lambda$ diagram for the spherical cap shown in Fig. 22.

The fact that the bifurcation point, which represents the stability limit, is very close to the snap-through point has aroused interest in the relevant snap-through mode in the framework of the CLE, see Fig. 7(b). Fig. 26(a) shows the eigenform concerned, for $\lambda = 0$. Fig. 26(b) illustrates this eigenform for $\lambda = 5.364$, i.e. just before the stability limit. The plus sign in the color scales refers to displacements in the inward direction of the undeformed shell and the minus sign to displacements in the outward direction.

Fig. 27 illustrates the λ_1^*–λ diagram and the λ_2^*–λ diagram for the spherical cap. The detail indicates that the bifurcation point precedes the snap-through point. Remarkably, with the exception of a very small subregion immediately before the bifurcation point, $\lambda_1^* - \lambda > \lambda_2^* - \lambda$, giving the incorrect impression that loss of stability will occur by bifurcation buckling.

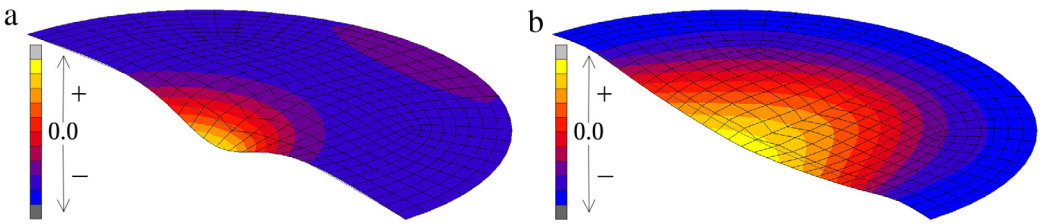

Fig. 26. Eigenform referring to the relevant snap-through mode for (a) $\lambda = 0$ and (b) $\lambda = 5.364$.

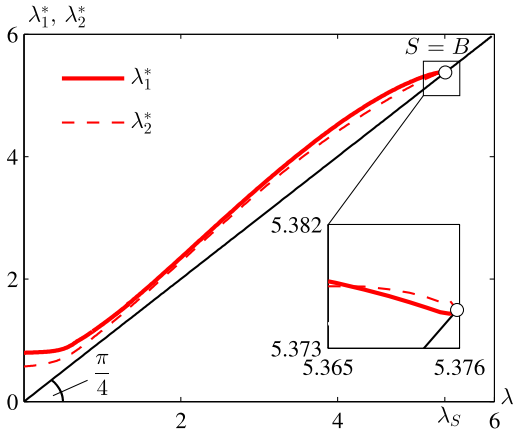

Fig. 27. λ_1^*–λ diagram and λ_2^*–λ diagram for the spherical cap shown in Fig. 22.

For the exceptional case of hilltop buckling, characterized by the coincidence of the bifurcation point and the snap-through point,

$$\lambda_{,\xi}(\lambda_S) = 0, \qquad \lambda_{1,\xi}^*(\lambda_S) = \lambda_{2,\xi}^*(\lambda_S) = 0 \implies \dot{\lambda}_1^*(\lambda_S) = \dot{\lambda}_2^*(\lambda_S) = -1. \tag{105}$$

This exceptional case contains two fundamental eigenpairs: $(\lambda_1^*(\lambda) - \lambda, \mathbf{v}_1^*(\lambda))$ and $(\lambda_2^*(\lambda) - \lambda, \mathbf{v}_2^*(\lambda))$. $(U - U_M)/U$ must obviously be the same for these two eigenpairs. Thus, as far as the hypothesis for $(U - U_M)/U$ is concerned,

$$\sqrt{\rho_1^2(\lambda) + c_1^2(\lambda)\left(1 - \rho_1^2(\lambda)\right)} = \sqrt{\rho_2^2(\lambda) + c_2^2(\lambda)\left(1 - \rho_2^2(\lambda)\right)}, \tag{106}$$

as follows from Eq. (41). At the stability limit,

$$\rho_1(\lambda_S) = \rho_2(\lambda_S) = 0, \tag{107}$$

see Eq. (15.2), resulting in

$$c_1(\lambda_S) = c_2(\lambda_S), \tag{108}$$

see Eq. (43). $c_1(\lambda_S)$ and $c_2(\lambda_S)$ are indeterminate forms, referring to bifurcation buckling and snap-through, respectively. Moreover, since both eigenpairs must provide the same vector $\mathbf{a}(\theta(\lambda), \varphi(\lambda))$,

$$\varphi_1(\lambda) = \varphi_2(\lambda), \tag{109}$$

which requires

$$\mathbf{v}_{10}^* \cdot \mathbf{v}_1^*(\lambda) = \mathbf{v}_{20}^* \cdot \mathbf{v}_2^*(\lambda), \tag{110}$$

see Eq. (3).

Fig. 28 illustrates the curve $\mathbf{a}(\theta(\lambda), \varphi(\lambda))$ on the surface of the buckling sphere for the spherical cap. The angle $\theta(\lambda)$ was obtained in a conventional manner. The initial increase of the angle θ indicates a weaker increase of the membrane energy with increasing angle φ than of its energetical complement. Relatively close to the buckling meridian $\theta(\lambda)$ becomes a maximum, which signals a maximum value of the "non-membrane" percentage energy. Thereafter, the percentage membrane energy increases. At the stability limit the surface curve is tangent to the buckling meridian, which is very close to the meridian containing the *infinity point*, as follows from

$$\cos\,\varphi(\lambda_S) = \mathbf{v}_{10}^* \cdot \mathbf{v}_1^*(\lambda_S) = 0.00513. \tag{111}$$

This is consistent with the pronounced nonlinearity of the λ–w diagrams, see Fig. 23(a), and the large value of $w(\lambda_S)$ in comparison to the rise f of the shell, namely

$$w(\lambda_S)\,/\,f \approx 1.51, \tag{112}$$

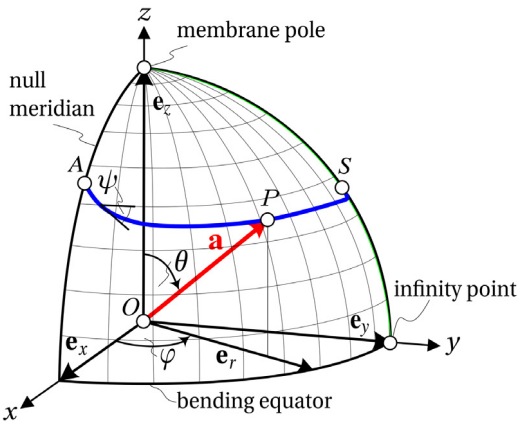

Fig. 28. $\mathbf{a}(\theta(\lambda), \varphi(\lambda))$ for a general stress state, as obtained for the spherical cap shown in Fig. 22.

see Figs. 22 and 23(a). The zenith angle of the points on the surface curve $\mathbf{a}(\theta(\lambda), \varphi(\lambda))$ in Fig. 28 is remarkably smaller than the one in Fig. 21. The reason for this is the ability of the shell to carry a concentrated load by stimulating a significantly higher percentage of membrane action than the arch. Such a load leads to considerable bending only in the neighborhood of its point of application.

10. Conclusions

- The hypothesized key role of the CLE in the concept of the buckling sphere was verified numerically.
- In particular, it was shown that the fundamental eigenpair $(\lambda_1^* - \lambda, \mathbf{v}_1^*)$ of the CLE stands out from the remaining $N-1$ eigenpairs of a system with N degrees of freedom, representing the FE-discretization of an elastic structure.
- E.g., irrespective of the type of the stability limit, $\lambda_{1,\xi}^* = 0$, $\mathbf{v}_{1,\xi}^* = \mathbf{0}$ at this point, indicating that it is a singular point of $\mathbf{v}_1^*(\lambda)$. A stability limit in the form of a snap-through point correlates with an N-fold null eigenvalue of the CLE. However, in contrast to $\lambda_{1,\xi}^* = 0$, $\lambda_{j,\xi}^* \neq 0$, $j = 2, 3, \ldots, N$, at such a point.
- $\cos\,\varphi(\lambda) = \mathbf{v}_1^*(0) \cdot \mathbf{v}_1^*(\lambda) < 0$ signals the impossibility of a stability limit in the form of a snap-through point. This was the rationale for the restriction of the numerical investigation to an octant of the unit sphere. The only type of stability limits that is not captured because of this restriction are bifurcation points that coincide with saddle points of load–displacement paths.
- The magnitude of $\varphi(\lambda)$ at the stability limit was found to correlate with a global quantity that depends on both the "non-membrane" deformations and of the stiffness of the structure at incipient buckling.
- It was also shown that the CLE can produce a constant fundamental eigenvector that corresponds to a nonlinearly varying fundamental eigenvalue.
- This proof was the theoretical prerequisite for the numerical verification of the hypothesized constancy of $\mathbf{v}_1^*$ for the limiting case of buckling from a membrane stress state.
- This verification was then the prerequisite for the formulation of a general CLE-based hypothesis for $(U - U_M)/U$. It was verified exactly for the limiting case of buckling from a membrane stress state and approximately for the one of a pure bending stress state. From this it is concluded that the hypothesis is useful for a constant value of $(U - U_M)/U$ in the prebuckling region.
- The hypothesis involves the curvature and the twist of a fictitious surface curve, described by the vertex of the unit vector $\mathbf{v}_1^*$. The fact that it is not a vector in a physical sense was no impediment to the use of differential geometry to determine these geometric quantities.
- For the case of buckling from a general stress state, the hypothesis was checked by comparing the result for $(U - U_M)/U$ of one of the two examples with the one obtained by means of a conventional computation of this ratio. Lack of agreement of the results for this problem was the reason for computing the zenith angle for the last example in a conventional manner.
- This falsification of the hypothesis is not crucial to the concept of the buckling sphere, because both the *membrane pole* and the *bending equator* as well as the *infinity point* and the *buckling meridian* are captured by the CLE,

whereas the zenith angle for the case of a general stress state can alternatively and more conveniently be computed in a conventional way.

- A challenging task of this work was the numerical realization of the concept of the buckling sphere.
- What has rendered it relatively difficult, was the need to compute derivatives of matrices and vectors with respect to the load parameter. The analytical computation of the coefficient matrices $\widetilde{\mathbf{K}}_T$ and $\widetilde{\widetilde{\mathbf{K}}}_T$ in the mathematical formulation of the CLE for the special case of a plane, co-rotational finite beam element was important in its own right. Moreover, it proved to be useful for verifying the solution of the CLE, obtained with the help of the commercial software MSC.MARC, where $\widetilde{\widetilde{\mathbf{K}}}_T$ was approximated by a finite-difference expression.
- To achieve the desired accuracy of the finite-difference approximation of $\dot{\mathbf{v}}_1^*(\lambda)$, several subroutines of MSC.MARC had to be modified.
- The interaction of problem-specific software, written in the course of the present research project, with MSC.MARC has proved to be very good.
- Part of the numerical findings is seen as quantitative corroborations of traditional qualitative dicta, such as "a structure with a lot of bending", "a significant redistribution of stresses", etc.
- The buckling sphere is the object of a remarkable symbiosis of mechanics and geometry. The scientific preoccupation with this object is a good example of a symbiosis of more general nature, namely, of the one of fundamental and applied research, which is a trademark of the engineering sciences.

11. Epilog

Analogous to a well-known motto of ceiling paintings about the relation between science and faith, the elaborated symbiosis of mechanics and geometry may be characterized by the following dictum: *mechanica et geometria, quam bene conveniunt* [in Latin: mechanics and geometry, how well they get along].

Acknowledgment

The junior authors gratefully acknowledge financial support of the research project Categorization of buckling by means of spherical geometry (P24526-N26) by the Austrian Science Fund (FWF).

Appendix A. Determination of $\rho(\lambda)$ and $c^2(\lambda)(1-\rho^2(\lambda))$

The hypothesis for $(U-U_M)/U$, see Eq. (41), contains the functions $\rho(\lambda)$ and $c(\lambda)$.
To determine $\rho(\lambda)$,

$$\mathbf{v}_1^*(\lambda)\cdot\mathbf{v}_1^*(\lambda)=1,\quad \lambda=\lambda(\xi), \tag{A.1}$$

is differentiated with respect to ξ. Reasons for choosing ξ as the parameter are that $\mathrm{d}\xi(\lambda)>0$ includes the stability limit even if it is a snap-through point and that the equation of definition for $c^2(\lambda)(1-\rho^2(\lambda))$, see Eq. (A.16), contains the term $\rho_{,\xi}$. It is repeated here that $\mathbf{v}_1^*(\lambda)$ is not a vector in a physical sense and that its position relative to the three coordinate axes of a Cartesian system of reference is irrelevant to the following determination of $\rho(\lambda)$ by means of differential geometry. The said differentiation gives

$$\mathbf{v}_1^*\cdot\mathbf{v}_{1,\xi}^*=0. \tag{A.2}$$

$\mathbf{v}_{1,\xi}^*$ is a vector tangent to the fictitious surface curve, described by the vertex of $\mathbf{v}_1^*(\lambda)$ unless, of course, $\mathbf{v}_{1,\xi}^*=\mathbf{0}$, as it may at a singular point [11]. Interpreting ξ as the time,

$$\mathbf{v}_{1,\xi}^*=v\cdot\mathbf{t} \tag{A.3}$$

represents the vector velocity of a particle moving on this curve. Its absolute value,

$$v=\|\mathbf{v}_{1,\xi}^*\| \tag{A.4}$$

is the speed of the particle; $\mathbf{t}$ denotes the tangent vector, which is a unit vector. Substitution of Eq. (A.3) into Eq. (A.2) yields

$$v\,(\mathbf{v}_1^*\cdot\mathbf{t})=0. \tag{A.5}$$

At a regular point of the fictitious surface curve,

$$v > 0, \quad \mathbf{v}_1^* \cdot \mathbf{t} = 0. \tag{A.6}$$

At the stability limit, which is a singular point, where $\mathbf{t}$ is not defined,

$$v = 0, \tag{A.7}$$

as follows from Eq. (93). At such a point, $v(\xi)$ is not smooth. Hence, $v_{,\xi}(\xi)$ is not defined. However,

$$\lim_{\Delta\xi \to 0} v_{,\xi}(\xi_S + \Delta\xi) = -\lim_{\Delta\xi \to 0} v_{,\xi}(\xi_S - \Delta\xi) > 0, \tag{A.8}$$

where $v_{,\xi}(\xi_S + \Delta\xi)$ is interpreted as the tangent acceleration of a particle at $\xi_S + \Delta\xi$. The special case

$$v(\lambda) = 0 \tag{A.9}$$

is characterized by

$$\mathbf{v}_1^*(\lambda) = \mathbf{const}. \tag{A.10}$$

Derivation of Eq. (A.2) with respect to ξ results in

$$\mathbf{v}_{1,\xi}^* \cdot \mathbf{v}_{1,\xi}^* + \mathbf{v}_1^* \cdot \mathbf{v}_{1,\xi\xi}^* = 0. \tag{A.11}$$

$\mathbf{v}_{1,\xi\xi}^*$ is interpreted as the vector acceleration, given as [11]

$$\mathbf{v}_{1,\xi\xi}^* = v_{,\xi}\mathbf{t} + \frac{v^2}{\rho}\mathbf{n}. \tag{A.12}$$

$\mathbf{n}$ denotes the principal normal vector, which is a unit vector, normal to $\mathbf{t}$; v^2/ρ is the normal acceleration. Substitution of Eqs. (A.3) and (A.12) into Eq. (A.11) and consideration of Eq. (A.6.2) yields

$$v^2 \left(1 + \frac{\mathbf{v}_1^* \cdot \mathbf{n}}{\rho}\right) = 0. \tag{A.13}$$

At a regular point of the fictitious surface curve,

$$\boxed{v > 0, \quad 0 < \rho = -\mathbf{v}_1^* \cdot \mathbf{n} < 1}. \tag{A.14}$$

At the stability limit,

$$\boxed{v = 0, \qquad \rho = 0}. \tag{A.15}$$

Fig. 29 shows that $\alpha = \arccos \rho$, see Eq. (42), is the angle enclosed by the vectors $\mathbf{v}_1^*$ and $-\mathbf{n}$, which are located in a plane normal to $\mathbf{t}$.

The rationale behind the term $c^2(1-\rho^2)$ in the hypothesis for $(U - U_M)/U$, see Eq. (41), was to avoid that, following from $\rho(\lambda_S) = 0$, irrespective of the stress state at the stability limit, $U(\lambda_S) = U_M(\lambda_S)$. The starting point for determination of $c^2(\lambda)(1-\rho^2)$ is the following equation of definition:

$$c^2(\lambda)(1 - \rho^2(\lambda)) := \left(\sigma(\lambda)\rho_{,\xi}\right)^2 \left(\frac{\lambda_{,\xi}}{\lambda_1^* - \lambda}\right)^2, \tag{A.16}$$

where

$$\sigma \equiv \frac{1}{\tau}. \tag{A.17}$$

$\tau(\lambda)$ is the twist of the aforementioned fictitious surface curve, $\lambda_1^*(\lambda) - \lambda$ is the fundamental eigenvalue of the CLE, and $\rho_{,\xi}(\lambda)$ is the derivative of $\rho(\lambda)$ with respect to ξ. It follows from Eq. (A.14.2) as

$$\rho_{,\xi} = -\mathbf{v}_{1,\xi}^* \cdot \mathbf{n} - \mathbf{v}_1^* \cdot \mathbf{n}_{,\xi}, \tag{A.18}$$

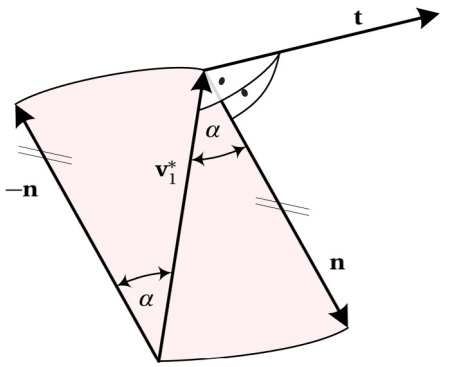

Fig. 29. Illustration of $\cos\alpha = -\mathbf{v}_1^* \cdot \mathbf{n} = \rho$.

where

$$\mathbf{n}_{,\xi} = \frac{\mathrm{d}\mathbf{n}}{\mathrm{d}s}\frac{\mathrm{d}s}{\mathrm{d}\xi} = \frac{\mathrm{d}\mathbf{n}}{\mathrm{d}s} \cdot v \tag{A.19}$$

with

$$\frac{\mathrm{d}\mathbf{n}}{\mathrm{d}s} = -\kappa\mathbf{t} + \tau\mathbf{b} \tag{A.20}$$

as the 2nd *Frenet* formula [16], where ds is an infinitesimal increment of the arc length of the fictitious surface curve; $\mathbf{b}$ denotes the binormal vector, which is a unit vector, normal to $\mathbf{t}$ and $\mathbf{n}$. Substitution of Eq. (A.20) into Eq. (A.19) and insertion of the result and of Eq. (A.3) into Eq. (A.18) yields

$$\rho_{,\xi} = -v\,(\mathbf{t}\cdot\mathbf{n}) - v\mathbf{v}_1^*\,(-\kappa\mathbf{t} + \tau\mathbf{b}). \tag{A.21}$$

Making use of the orthogonality of $\mathbf{t}$ with respect to both $\mathbf{n}$ and $\mathbf{v}_1^*$, see Fig. 29, results in

$$\sigma\rho_{,\xi} = -v(\mathbf{v}_1^* \cdot \mathbf{b}). \tag{A.22}$$

It is worth of mention that for $\rho_{,\xi} = 0$, $\sigma = \infty$. Thus, $\sigma\rho_{,\xi}$ becomes an indefinite form, the value of which is equal to $-v(\mathbf{v}_1^* \cdot \mathbf{b})$. Substitution of Eq. (A.22) into Eq. (A.16) gives

$$c^2(\lambda)(1-\rho^2(\lambda)) = \left(\frac{v\,\lambda_{,\xi}}{\lambda_1^* - \lambda}\right)^2 \left(-\mathbf{v}_1^* \cdot \mathbf{b}\right)^2. \tag{A.23}$$

Since $\mathbf{v}_1^*$ is located in the normal plane, spanned by the unit vectors $\mathbf{n}$ and $\mathbf{b}$,

$$(\mathbf{v}_1^* \cdot \mathbf{n})^2 + (\mathbf{v}_1^* \cdot \mathbf{b})^2 = 1. \tag{A.24}$$

Thus,

$$(\mathbf{v}_1^* \cdot \mathbf{b})^2 = 1 - (\mathbf{v}_1^* \cdot \mathbf{n})^2 = 1 - \rho^2 = \sin^2\alpha. \tag{A.25}$$

Substitution of Eq. (A.25) into Eq. (A.23) shows that

$$c^2(\lambda) = \left(\frac{v\,\lambda_{,\xi}}{\lambda_1^* - \lambda}\right)^2, \tag{A.26}$$

which agrees with Eq. (43). Fig. 30 serves the purpose to determine the sign of $\mathbf{v}_1^* \cdot \mathbf{b}$ before and after the stability limit.

At the stability limit $P = S$, which is a singular point of $\mathbf{v}_1^*(\lambda)$, a reversal of the directions of $\mathbf{t}$ and $\mathbf{b}$ as a result of rotating 180° around $\mathbf{n}$ occurs. This produces a change of the value of $\mathbf{v}_1^* \cdot \mathbf{b}$ at this point from -1 to $+1$, recalling that $|\sin\alpha(\lambda_S)| = 1$. For $0 \le \lambda < \lambda_S$, $\mathbf{v}_1^* \cdot \mathbf{b} = -\sin\alpha < 0$, see Fig. 30(a), and $\lambda_{,\xi}/(\lambda_1^* - \lambda) > 0$ with $\lambda_1^* - \lambda > 0$

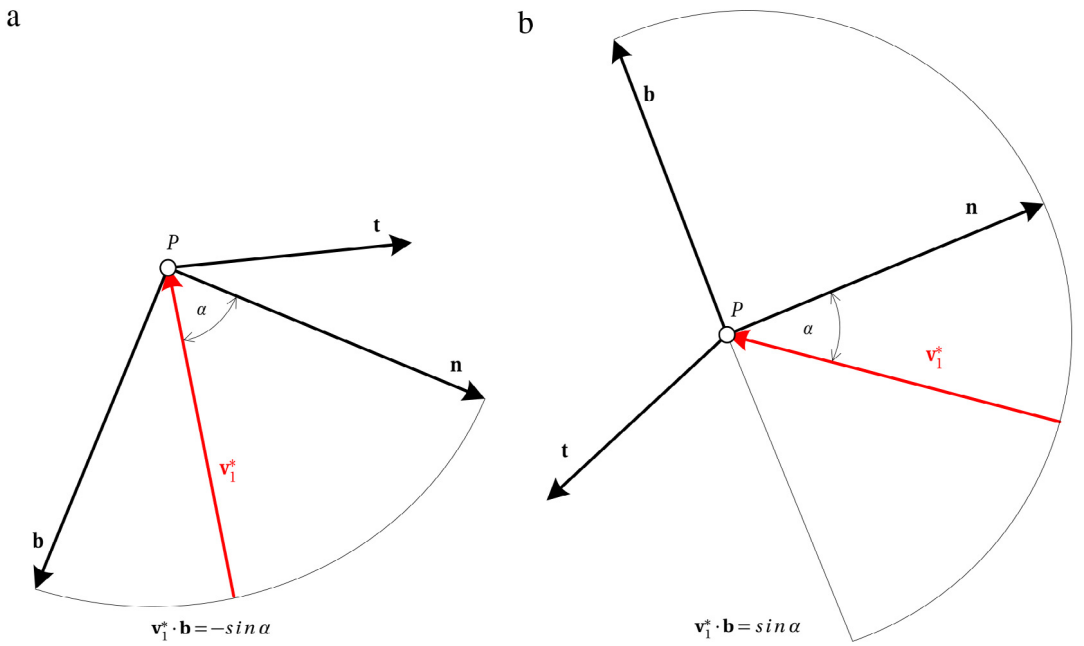

Fig. 30. On determination of the sign of $\mathbf{v}_1^* \cdot \mathbf{b}$ for (a) $0 \leq \lambda < \lambda_S$, (b) $\lambda > \lambda_S$.

and $\lambda_{,\xi} > 0$. For $\lambda > \lambda_S$, $\mathbf{v}_1^* \cdot \mathbf{b} = \sin\alpha > 0$, see Fig. 30(b), and $\lambda_{,\xi}/(\lambda_1^* - \lambda) < 0$. In case of bifurcation buckling, $\lambda_1^* - \lambda < 0$, see Fig. 13(a), and $\lambda_{,\xi} > 0$, whereas for snap-through, $\lambda_1^* - \lambda > 0$, see Fig. 7(a), and $\lambda_{,\xi} < 0$. In any case,

$$c\sqrt{1-\rho^2} = \frac{v\,\lambda_{,\xi}}{\lambda_1^* - \lambda}(-\mathbf{v}_1^* \cdot \mathbf{b}) \geq 0. \tag{A.27}$$

For the limiting case of a membrane stress state, $v(\lambda) = 0$, see Eq. (45), which follows from the constancy of $\mathbf{v}_1^*(\lambda)$ for this special case. Substitution of Eq. (45) into Eq. (A.26) yields

$$c(\lambda) = 0. \tag{A.28}$$

Hence, the result for $c(\lambda)$ does not depend on the factor $\lambda_{,\xi}/(\lambda_1^* - \lambda)$ in Eq. (A.27). For all other stress states, however, this is not the case. To check the situation at the stability limit, Eq. (41) is specialized for this singular point of $\mathbf{v}_1^*(\lambda)$. Thus, following from Eq. (A.15.2),

$$\rho(\lambda_S) = 0. \tag{A.29}$$

Substitution of Eq. (A.29) into Eq. (41) results in

$$\left.\frac{U - U_M}{U}\right|_{\lambda=\lambda_S} = c(\lambda_S). \tag{A.30}$$

Irrespective of the type of the stability limit,

$$\lambda_1^*(\lambda_S) - \lambda_S = 0, \qquad v(\lambda_S) = 0. \tag{A.31}$$

However, for bifurcation buckling, $\lambda_{,\xi}(\lambda_S) > 0$, whereas for snap-through, $\lambda_{,\xi}(\lambda_S) = 0$. A necessary condition for the usefulness of the aforementioned factor is the receipt of the same formula for $c(\lambda_S)$ for both types of loss of stability. To verify this condition, Eq. (A.26) is specialized for the stability limit, which gives

$$c(\lambda_S) = \frac{v\,\lambda_{,\xi}}{\lambda_1^* - \lambda} = \frac{0 \cdot \lambda_{,\xi}}{0}, \tag{A.32}$$

where use of Eq. (A.31) was made. Application of *de L'Hospital's* rule to the above indefinite form gives

$$c(\lambda_S) = -\frac{v_{,\xi}\,\lambda_{,\xi} + v\,\lambda_{,\xi\xi}}{\lambda^*_{1,\xi} - \lambda_{,\xi}}, \tag{A.33}$$

where

$$v_{,\xi} := \lim_{\Delta\xi\to 0} v_{,\xi}(\xi_S - \Delta\xi) = -\lim_{\Delta\xi\to 0} v_{,\xi}(\xi_S + \Delta\xi) \le 0, \tag{A.34}$$

recalling that $v = \|\mathbf{v}^*_{1,\xi}(\xi)\|$ is not smooth at a singular point of $\mathbf{v}^*_1(\lambda)$. Irrespective of the type of the stability limit,

$$\lambda^*_{1,\xi}(\lambda_S) = 0. \tag{A.35}$$

Substitution of Eqs. (A.31.2) and (A.35) into Eq. (A.33) provides the result for loss of stability by bifurcation buckling:

$$c(\lambda_S) = -v_{,\xi} > 0. \tag{A.36}$$

For snap-through, the expression on the right-hand side of Eq. (A.33) is an indefinite form. With the help of *de L'Hospital's* rule and of

$$\frac{\lambda^*_{1,\xi\xi}}{\lambda_{,\xi\xi}} = -1, \tag{A.37}$$

see Eq. (62), $c(\lambda_S)$ is obtained as

$$c(\lambda_S) = -\frac{v_{,\xi\xi}\,\lambda_{,\xi} + 2v_{,\xi}\,\lambda_{,\xi\xi} + v\,\lambda_{,\xi\xi\xi}}{\lambda^*_{1,\xi\xi} - \lambda_{,\xi\xi}} = \frac{2v_{,\xi}\,\lambda_{,\xi\xi}}{-2\lambda_{\xi\xi}} = -v_{,\xi} > 0, \tag{A.38}$$

which agrees with Eq. (A.36). However, satisfaction of this necessary criterion for the general usefulness of the hypothesis for $(U - U_M)/U$ does not mean that the hypothesis is verified.

A physical interpretation of $v_{,\xi}(\lambda_S)$ according to Eq. (A.36) and Eq. (A.38), respectively, is the one of the tangent deceleration $\lim_{\Delta\xi\to 0} v_{,\xi}(\xi_S - \Delta\xi)$ of a particle, moving on the fictitious surface curve, which comes to rest at $\xi = \xi_S$. It is equal to the negative tangent acceleration $-\lim_{\Delta\xi\to 0} v_{,\xi}(\xi_S + \Delta\xi)$ of the particle when starting to move again. Obviously, this deceleration is a finite, negative quantity. Its upper bound, $v_{,\xi}(\lambda_S) = 0$, holds for the limiting case of a membrane stress state and its lower bound, $v_{,\xi}(\lambda_S) = -1$, for the one of a pure bending stress state. While the upper bound was confirmed numerically, this was not the case for the lower bound.

Appendix B. Numerical realization of the proposed concept

B.1. Consistently linearized eigenvalue problem

B.1.1. General remarks

An accurate and efficient solution of the CLE is a necessary condition for accomplishing the goal of a symbiosis of mechanics and geometry in the form of the buckling sphere. Originally, the CLE was used for *ab initio* estimates of stability limits by means of the FEM [1]. Later on, it was employed for assessing the initial postbuckling behavior of elastic structures [17–19]. In order to solve this linear eigenvalue problem, $\widetilde{\mathbf{K}}_T$ and $\overset{\sim}{\widetilde{\mathbf{K}}}_T$ must first be computed. For special types of finite elements, analytical expressions of the coefficients of $\widetilde{\mathbf{K}}_T(\lambda)$ are available. $\overset{\sim}{\widetilde{\mathbf{K}}}_T(\lambda)$ can then be computed by means of differentiation of these expressions [14]. In general, however, $\overset{\sim}{\widetilde{\mathbf{K}}}_T$ must be computed numerically with the help of the Finite Difference Method (FDM).

In this Subsection, at first, an analytical method of computation of the coefficient matrices of the CLE for a plane, co-rotational finite beam element will be presented. Thereafter, a general numerical method of computation of these matrices, based on a finite-difference approximation of $\overset{\sim}{\widetilde{\mathbf{K}}}_T$ and involving a commercial FE code, will be elaborated.

B.1.2. Analytical determination of $\widetilde{\mathbf{K}}_T$ and $\dot{\widetilde{\mathbf{K}}}_T$ and solution of the CLE

In the framework of the FEM, the tangent stiffness matrix $\widetilde{\mathbf{K}}_T$ of a system with N degrees of freedom is obtained by assembling the element tangent stiffness matrices $\widetilde{\mathbf{K}}_T^e$, $e = 1, 2, \ldots, M$, where M denotes the number of finite elements. For convenience's sake it is assumed that all elements have the same number, n, of degrees of freedom. Formally, this procedure can be described as follows:

$$\widetilde{\mathbf{K}}_T = \sum_{e=1}^{M} \mathbf{A}^e \cdot \widetilde{\mathbf{K}}_T^e \cdot \mathbf{A}^e. \tag{B.1}$$

In Eq. (B.1), $\mathbf{A}^e$ denotes the connectivity matrix of element e. Since the connectivity matrices are constant,

$$\dot{\widetilde{\mathbf{K}}}_T = \sum_{e=1}^{M} \mathbf{A}^e \cdot \dot{\widetilde{\mathbf{K}}}_T^e \cdot \mathbf{A}^e. \tag{B.2}$$

Hence, instead of differentiation of the $N \times N$ matrix $\widetilde{\mathbf{K}}_T$ with respect to λ, it is sufficient to derive the analytical expressions for the coefficients of the $n \times n$ matrix $\widetilde{\mathbf{K}}_T^e$ with respect to this parameter. Thereafter, the matrices $\dot{\widetilde{\mathbf{K}}}_T^e$ are assembled to the matrix $\dot{\widetilde{\mathbf{K}}}_T$.

The matrix $\widetilde{\mathbf{K}}_T^e$ of a co-rotational finite beam element, based on the Euler–Bernoulli assumptions, is given as [14]

$$\widetilde{\mathbf{K}}_T^e = \mathbf{X} \cdot \bar{\mathbf{K}}_T^e \cdot \mathbf{X} + \frac{\mathbf{z} \otimes \mathbf{z}}{\hat{l}} \bar{N} + \frac{(\mathbf{r} \otimes \mathbf{z} + \mathbf{z} \otimes \mathbf{r})(\bar{M}_1 + \bar{M}_2)}{\hat{l}^2}, \tag{B.3}$$

where $\mathbf{X}$ denotes the matrix for the transformation of the element stiffness matrix in the local coordinate system, $\bar{\mathbf{K}}_T^e$, from local to global coordinates; $\hat{l}$ is the length of the cord of the deformed beam element; the vectors $\mathbf{r}$, $\mathbf{z}$ represent abbreviations of lengthy expressions, given in [14]; $\bar{M}_1$, $\bar{M}_2$, $\bar{N}$ denote the components of the force vector in this coordinate system. In the above expression for $\widetilde{\mathbf{K}}_T^e$ the superscript e was suppressed, with exception of $\bar{\mathbf{K}}_T^e$. Differentiation of Eq. (B.3) with respect to λ yields

$$\begin{aligned}\dot{\widetilde{\mathbf{K}}}_T^e = {} & \dot{\mathbf{X}} \cdot \bar{\mathbf{K}}_T^e \cdot \mathbf{X} + \mathbf{X} \cdot \dot{\bar{\mathbf{K}}}_T^e \cdot \mathbf{X} + \mathbf{X} \cdot \bar{\mathbf{K}}_T^e \cdot \dot{\mathbf{X}} + \frac{(\dot{\mathbf{z}} \otimes \mathbf{z} + \mathbf{z} \otimes \dot{\mathbf{z}})\hat{l} - \mathbf{z} \otimes \mathbf{z}\dot{\hat{l}}}{\hat{l}^2} \bar{N} + \frac{\mathbf{z} \otimes \mathbf{z}}{\hat{l}} \dot{\bar{N}} \\ & + \frac{(\dot{\mathbf{r}} \otimes \mathbf{z} + \mathbf{r} \otimes \dot{\mathbf{z}} + \dot{\mathbf{z}} \otimes \mathbf{r} + \mathbf{z} \otimes \dot{\mathbf{r}})\hat{l}^2}{\hat{l}^2} (\bar{M}_1 + \bar{M}_2) - \frac{2(\mathbf{r} \otimes \mathbf{z} + \mathbf{z} \otimes \mathbf{r})\dot{\hat{l}}}{\hat{l}^3} (\bar{M}_1 + \bar{M}_2) \\ & + \frac{\mathbf{r} \otimes \mathbf{z} + \mathbf{z} \otimes \mathbf{r}}{\hat{l}^2} (\dot{\bar{M}}_1 + \dot{\bar{M}}_2).\end{aligned} \tag{B.4}$$

Knowledge of $\dot{\widetilde{\mathbf{K}}}_T^e$ paves the way for the solution of the CLE, which is obtained by means of the commercial software *MATLAB*.

B.1.3. Numerical determination of $\widetilde{\mathbf{K}}_T$ and $\dot{\widetilde{\mathbf{K}}}_T$ and solution of the CLE

Determination of the tangent stiffness matrix $\widetilde{\mathbf{K}}_T$ for distinct values of λ is part of a standard incremental–iterative nonlinear structural analysis by the FEM. Herein, such an analysis is performed with the help of the commercial software MSC.MARC [20]. This is done *before* the numerical solution of the CLE for the selected values of λ.

The mathematical formulation of the CLE contains the matrix $\dot{\widetilde{\mathbf{K}}}_T(\mathbf{q}(\lambda))$. The starting point of the algorithm for determination of this matrix for a specific value of λ is the differential form of the equilibrium equations for the discretized structure:

$$\widetilde{\mathbf{K}}_T \cdot d\mathbf{q} = d\lambda \cdot \bar{\mathbf{P}}. \tag{B.5}$$

Replacing $d\mathbf{q}$ and $d\lambda$ by the finite increments $\Delta\mathbf{q}$ and $\Delta\lambda$ yields

$$\widetilde{\mathbf{K}}_T \cdot \Delta\mathbf{q} = \Delta\lambda \cdot \bar{\mathbf{P}}. \tag{B.6}$$

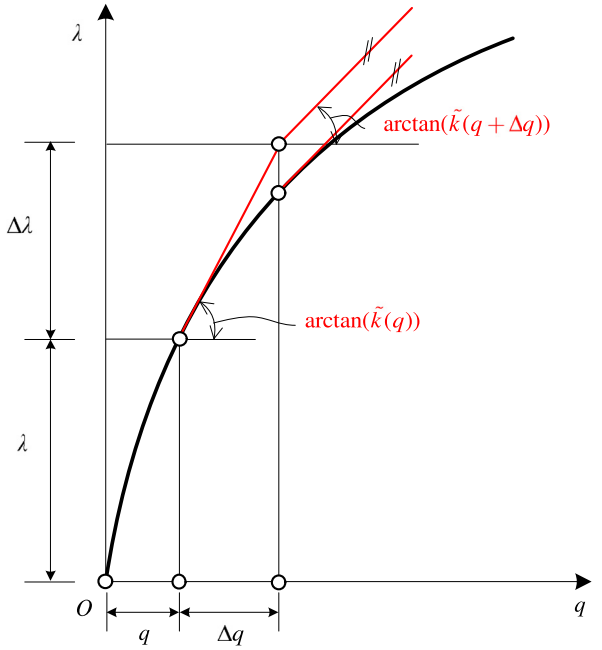

Fig. 31. On the approximation of $\dot{\tilde{\mathbf{K}}}_T(\mathbf{q})$ by a forward finite-difference expression for the special case of a one degree-of-freedom system.

Solving Eq. (B.6) for $\Delta\mathbf{q}$ enables computation of $\mathbf{K}_T(\mathbf{q}+\Delta\mathbf{q})$, where the absence of the tilde indicates that this matrix does not refer to an equilibrium state. Knowledge of $\mathbf{K}_T(\mathbf{q}+\Delta\mathbf{q})$ allows computation of an approximation of $\dot{\tilde{\mathbf{K}}}_T(\mathbf{q})$ by a forward finite-difference expression, given as

$$\dot{\mathbf{K}}_T(\mathbf{q}) = \frac{\mathbf{K}_T(\mathbf{q}+\Delta\mathbf{q}) - \tilde{\mathbf{K}}_T(\mathbf{q})}{\Delta\lambda}. \tag{B.7}$$

Fig. 31 illustrates the described situation for the special case of a one degree-of-freedom system, for which Eq. (B.7) degenerates to

$$\dot{k}_T(q) = \frac{k_T(q+\Delta q) - \tilde{k}_T(q)}{\Delta\lambda}. \tag{B.8}$$

Both the accuracy and the efficiency of the forward finite-difference scheme are high [21], as will be confirmed later.

Computation of $\Delta\mathbf{q}$ is an ingredient of the first iteration step in the framework of incremental–iterative FE analysis by the Newton–Raphson method for the increment $\Delta\lambda$. This step is carried out by MSC.MARC. Knowledge of $\Delta\mathbf{q}$ is a prerequisite for solving the CLE for a first approximation of the eigenpair $(\lambda_1^*(\lambda) - \lambda, \mathbf{v}_1^*(\lambda))$, denoted as $(\lambda_{1(0)} - \lambda, \mathbf{v}_{1(0)}(\lambda))$. This is done with the help of *MATLAB*. However, a single approximation of this eigenpair does not allow to assess its accuracy. In order to obtain an approximation of the fundamental eigenpair which satisfies a prespecified requirement of accuracy, additional approximations of this eigenpair are necessary. They are based on several sets of reductions of the original size of the increment $\Delta\lambda$. In Appendix C it is shown how to compute a sufficiently accurate approximation of the fundamental eigenpair.

Table 3 contains a set of values of the quantity

$$\left| \frac{\lambda_1^*(FE_{v2}) - \lambda_1^*(FD)}{\lambda_1^*(FE_{v2})} \right|, \tag{B.9}$$

obtained for a two-hinged arch, subjected to a point load at the apex [14]. $\lambda_1^*(FD)$ refers to the results obtained with the help of the numerical approach proposed in this part of Appendix B.1, considering Appendix C, whereas $\lambda_1^*(FE_{v2})$ concerns the results obtained by means of the analytical approach, described in the preceding part of this Appendix. The same type of finite element (element #95 in [12]) was used for both methods. The maximum difference of the results is less than 2%. It occurs for $\lambda = 0$. In general, the difference is less than 1%.

Table 3
$\left|\left(\lambda_1^*(FE_{v2}) - \lambda_1^*(FD)\right)/\lambda_1^*(FE_{v2})\right|$ for different values of λ/λ_S.

	λ/λ_S										
	0.0	0.1	0.2	0.3	0.4	0.5	0.6	0.7	0.8	0.9	1.0
$\left\lvert\frac{\lambda_1^*(FE_{v2})-\lambda_1^*(FD)}{\lambda_1^*(FE_{v2})}\right\rvert$	0.0185	0.0017	0.0116	0.0018	0.0029	0.0086	0.0073	0.0051	0.0023	0.0010	0.0020

B.2. Numerical determination of $\rho(\lambda)$ and $c(\lambda)$

The hypothesis for $(U - U_M)/U$ according to Eq. (41) contains $\rho(\lambda)$ and $c(\lambda)$. $\rho(\lambda)$ is given as

$$\frac{1}{\kappa(\lambda)} \equiv \rho(\lambda) = -\mathbf{v}_1^*(\lambda) \cdot \mathbf{n}(\lambda), \tag{B.10}$$

see Eq. (42), with $\mathbf{n}(\lambda)$ as the principal normal vector of the previously mentioned fictitious surface curve, described by the vertex of $\mathbf{v}_1^*(\lambda)$. Computation of $\mathbf{v}_1^*(\lambda)$ is part of the solution of the CLE, which was the topic of Appendix B.1. $\mathbf{n}$ is defined as

$$\mathbf{n}(\lambda) = \frac{\dot{\mathbf{t}}(\lambda)}{|\dot{\mathbf{t}}(\lambda)|}, \tag{B.11}$$

where $\dot{\mathbf{t}}(\lambda)$ denotes the derivative of the tangent vector $\mathbf{t}(\lambda)$, which is a unit vector, with respect to λ. It is approximated by a central finite-difference expression, given as

$$\dot{\mathbf{t}}^{\square}(\lambda) = \frac{\hat{\mathbf{t}}(\lambda + \Delta\lambda) - \hat{\mathbf{t}}(\lambda - \Delta\lambda)}{2\Delta\lambda}, \tag{B.12}$$

where $\hat{\mathbf{t}}(\lambda + \Delta\lambda)$ and $\hat{\mathbf{t}}(\lambda - \Delta\lambda)$ are central finite-difference approximations of $\mathbf{t}(\lambda + \Delta\lambda)$ and $\mathbf{t}(\lambda - \Delta\lambda)$, obtained as

$$\hat{\mathbf{t}}(\lambda + \Delta\lambda) = \frac{\mathbf{v}_1^*(\lambda + 2\Delta\lambda) - \mathbf{v}_1^*(\lambda)}{2\Delta\lambda} \tag{B.13}$$

and

$$\hat{\mathbf{t}}(\lambda - \Delta\lambda) = \frac{\mathbf{v}_1^*(\lambda) - \mathbf{v}_1^*(\lambda - 2\Delta\lambda)}{2\Delta\lambda}, \tag{B.14}$$

respectively. The accuracy of the approximation $\rho^{\square}(\lambda)$ of $\rho(\lambda)$ depends on $\Delta\lambda$. By gradually reducing $\Delta\lambda$, the difference between $\rho^{\square}(\lambda)$ and $\rho(\lambda)$ decreases. If

$$\frac{\rho^{\square}_{(i)} - \rho^{\square}_{(i+1)}}{\rho^{\square}_{(i)}} < \epsilon, \tag{B.15}$$

where $\rho^{\square}_{(i)}$ and $\rho^{\square}_{(i+1)}$ are the results for $\rho^{\square}$ for two successive steps in the course of a gradual reduction of $\Delta\lambda$, and ϵ is a suitably chosen threshold value of the error tolerance, this process is terminated. On the other hand, $\Delta\lambda$ must be chosen large enough to avoid numerical problems when computing $\rho^{\square}(\lambda)$.

$c(\lambda)$ is obtained from Eq. (43), which contains $\lambda_1^*(\lambda) - \lambda$, $v(\lambda)$, and $\lambda_{,\xi}$. Computation of $\lambda_1^*(\lambda) - \lambda$ is part of the solution of the CLE, which was the topic of Appendix B.1. The approximation of $v(\lambda)$ is based on a central-difference expression for $\mathbf{v}_{1,\xi}^*(\lambda)$. $\lambda_{,\xi}(\xi)$ is approximated by replacing the infinitesimal increments $\mathrm{d}\lambda$ and $\mathrm{d}\xi$ by finite increments.

B.3. Conventional computation of $(U - U_M)/U$ for the example of a thin shell

Frequently, the contribution of the transverse shear deformations to the strain energy, stored in a thin shell, can be disregarded. In this case, U is equal to the sum of the membrane energy U_M and the bending energy U_B, i.e.

$$U = U_M + U_B. \tag{B.16}$$

U_M and U_B are given as

$$U_M = \int_A U_M^* \, dA \tag{B.17}$$

and

$$U_B = \int_A U_B^* \, dA, \tag{B.18}$$

where U_M^* and U_B^* are the membrane energy and the bending energy, respectively, per unit area of the middle surface of the undeformed shell. Based on the classical Love–Kirchhoff assumptions [22],

$$U_M^* = \frac{Eh}{2\,(1-\nu^2)} \left[(\varepsilon_\alpha^{(0)} + \varepsilon_\beta^{(0)})^2 - 2(1-\nu) \left(\varepsilon_\alpha^{(0)} \varepsilon_\beta^{(0)} - \frac{1}{4} \omega^{(0)2} \right) \right] \tag{B.19}$$

and

$$U_B^* = \frac{Eh^3}{24\,(1-\nu^2)} \left[(\chi_\alpha + \chi_\beta)^2 - 2(1-\nu)(\chi_\alpha \chi_\beta - \tau^2) \right], \tag{B.20}$$

where $\varepsilon_\alpha^{(0)}$, $\varepsilon_\beta^{(0)}$, $\omega^{(0)}$ are the membrane strains, χ_α, χ_β, τ are the changes of the curvatures and the twist, E is the modulus of elasticity and ν is Poisson's ratio of the material, for the sake of simplicity assumed to be isotropic, and h is the thickness of the shell; α and β denote orthogonal curvilinear coordinates, referred to the undeformed configuration of the shell. Strain–displacement equations were derived among others by Koiter [22]. His nonlinear shell theory takes the influence of the rotations about the tangents to the curvilinear parameter lines $\alpha = const.$ and $\beta = const.$ on the membrane strains into account.

Within the framework of the FEM, U_M and U_B are approximated as sums of the contributions of the individual finite elements, i.e.

$$U_M \approx \sum_{e=1}^{m} U_M^{(e)} \tag{B.21}$$

and

$$U_B \approx \sum_{e=1}^{m} U_B^{(e)}. \tag{B.22}$$

Details of the determination of $U_M^{(e)}$ and $U_B^{(e)}$ are given in [23].

A pseudo problem arises if arches and beams are treated as shells or folded plates. This is frequently the case in stability analyses of arches and beams with thin-walled cross-sections by means of the FEM. An example is an I-beam subjected to pure bending, see Fig. 32.

The strain energy is given as

$$U = \frac{1}{2} \int_V \sigma_x \varepsilon_x \, dV. \tag{B.23}$$

Substitution of

$$\sigma_x = \frac{M_y}{I_y} z, \tag{B.24}$$

where I_y is the moment of inertia of the cross-section of the beam about the y-axis, into Eq. (B.23) and use of Hooke's law results in

$$U = \frac{1}{2} \int \frac{M_y^2}{E I_y^2} z^2 \, dV = \frac{1}{2} \frac{M_y^2}{E I_y} l. \tag{B.25}$$

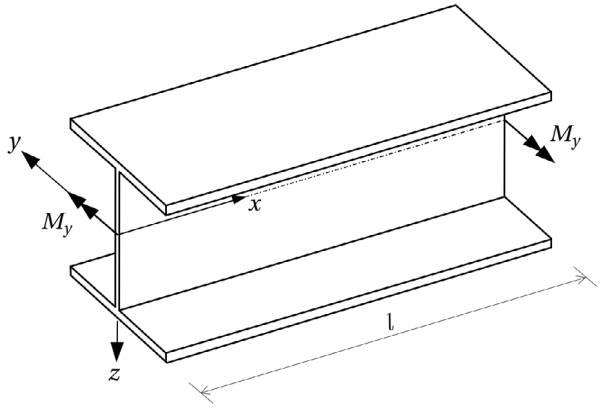

Fig. 32. I-beam subjected to pure bending about the y-axis.

Obviously,

$$U = U_B \implies U_M = 0. \tag{B.26}$$

If, however, the beam was analyzed as a folded plate, the strain energy would be obtained as the sum of the strain energies of the two flanges, $2U^{(F)}$, and of the web, $U^{(W)}$. Thus,

$$U = 2U^{(F)} + U^{(W)}, \tag{B.27}$$

where

$$U^{(F)} = U_M^{(F)} + U_B^{(F)} \tag{B.28}$$

and

$$U^{(W)} = U_M^{(W)}, \tag{B.29}$$

noting that $U_B^{(W)} = 0$ because σ_x is constant over the thickness of the web. Because of

$$U_M^{(F)} > 0, \qquad U_M^{(W)} > 0, \tag{B.30}$$

$U_M^{(F)} + U_M^{(W)}$ is not equal to U_M according to Eq. (B.26). The reason for the discrepancy is that computation of U on the basis of Eq. (B.27) does not consider Eq. (B.24), which is restricted to beam theory.

Modeling of beams as folded plates and shells will generally result in stress states that differ only very little from the ones obtained by means of beam theory. Otherwise its use would not be justified. Hence, it is the stress resultants of beam theory that are decisive for the decomposition of the strain energy in a membrane and a "non-membrane" part, notwithstanding that the stresses may have been computed by a two-dimensional theory. Contrary to Eqs. (B.17) and (B.18), the expressions for U_M and U_B represent line integrals along the beam axis. Conversely, "non-beam-like" folded plates and shells cannot be treated by beam theory. Consequently, it is the stress resultants of the two-dimensional theory in question that must be used for the aforementioned decomposition of the strain energy. Hence, there is no practical reason for concern about a possible non-uniqueness of this decomposition.

Appendix C. Numerical determination of the fundamental eigenpair

The error of the approximation of the fundamental eigenpair is first estimated for the largest increment $\Delta\lambda$, for which it is generally the largest. The size of $\Delta\lambda$ is chosen automatically by MSC.MARC. It is decreasing, as λ approaches the stability limit. Thus, if it turns out that the first approximation of the fundamental eigenpair is sufficiently accurate for the largest increment $\Delta\lambda$, it will, in general, be sufficiently accurate for the remaining load increments. In this case it would be sufficient to take the first approximations of the fundamental eigenpair for the individual load steps as the solution of the CLE.

Table 4
Checking of the relative accuracy of the substitute values of λ_1^* for increment #5 and of the accompanying approximations of $\mathbf{v}_1^*$.

	k	n_k	$\frac{\lambda_{1(n_k)} - \lambda_{1(n_{k-1})}}{\lambda_{1(n_{k-1})}}$	$1 - \mathbf{v}_{1(n_k)} \cdot \mathbf{v}_{1(n_k-1)}$
	1	$n_1 = 5$	–	$4.956 \cdot 10^{-8}$
$\frac{h_j}{\Delta\lambda^{(5)}} = 0.9^j$,	2	$n_2 = 10$	$8.4 \cdot 10^{-6}$	$1.717 \cdot 10^{-8}$
$j = 1, 2, \ldots, n_k$	3	$n_3 = 15$	$2.8 \cdot 10^{-6}$	$5.866 \cdot 10^{-9}$
	4	$n_4 = 20$	$1.2 \cdot 10^{-5}$	$1.923 \cdot 10^{-9}$

In order to estimate the error of the approximation of the fundamental eigenpair for the largest increment $\Delta\lambda$, substitute values of the unknown value of λ_1^* are computed and compared with each other. They are obtained through extrapolations in the framework of linear regression analysis. Each one of such analyses is based on a set of pairs of values $(h_j/\Delta\lambda,\ \lambda_{1(j)})$, $j = 1, 2, \ldots, n_k$, where $j = 0$ refers to $h_0 = \Delta\lambda$ and $\lambda_{1(0)}$, respectively, i.e. to the first approximation of λ_1^* (see Appendix B.1.3), and n_k denotes the number of pairs of values of set k.

To elucidate the procedure by means of an example treated in detail in Subchapter 9.2, four data sets are considered. The numbers of the respective pairs of values are chosen as $n_1 = 5,\ n_2 = 10,\ n_3 = 15,\ n_4 = 20$. Fig. 33 refers to the last data set. Accordingly, it shows 20 points, representing 20 different finite-difference approximations of λ_1^*, obtained as described in Appendix B.1.3. The superscript "5" in Fig. 33 indicates the increment considered. The subscript "19" refers to the largest refinement within this increment. $\lambda_{1(n_4)}^{(5)}$ denotes the substitute value of λ_1^*, obtained by means of data set n_4. By analogy, the remaining three substitute values of λ_1^*, i.e. $\lambda_{1(n_1)}^{(5)}$, $\lambda_{1(n_2)}^{(5)}$, $\lambda_{1(n_3)}^{(5)}$, are obtained.

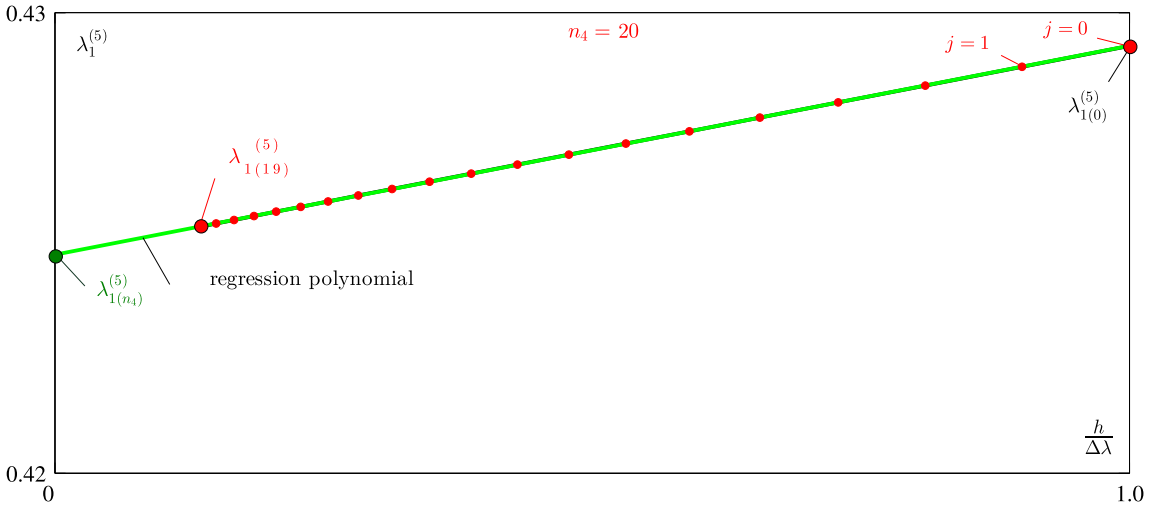

Fig. 33. Substitute value $\lambda_{1(n_4)}^{(5)}$ of λ_1^*, obtained with the data set $n_4 = 20$ for the largest increment $\Delta\lambda$ (increment #5).

Table 4 contains results from checking of the relative accuracy of the computed substitute values of λ_1^* for increment #5 and of the direction of the corresponding approximations of $\mathbf{v}_1^*$.

The results in the third column in Table 4 satisfy the condition

$$\frac{\lambda_{1(n_k)}^{(5)} - \lambda_{1(n_{k-1})}^{(5)}}{\lambda_{1(n_{k-1})}^{(5)}} < \epsilon_1 = 10^{-4}. \tag{C.1}$$

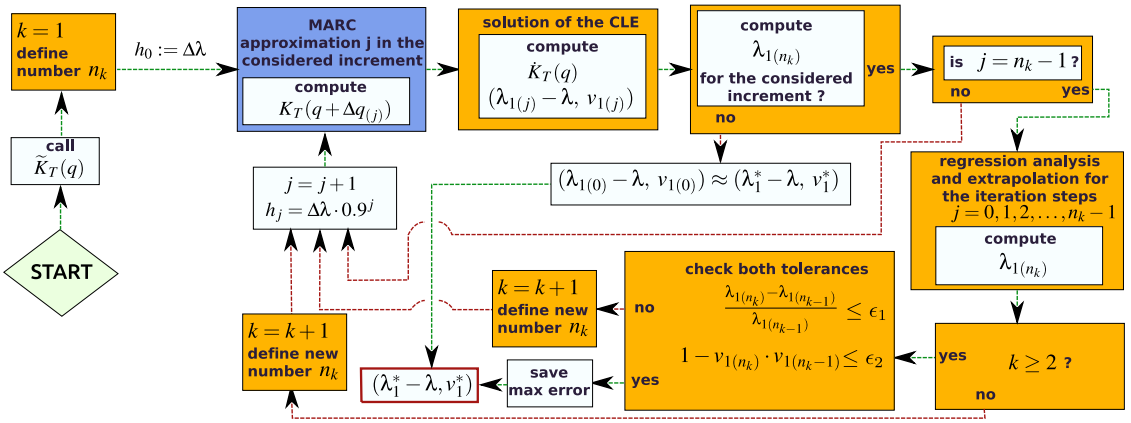

Fig. 34. Flowchart considering the numerical determination of the fundamental eigenpair for an arbitrary increment $\Delta\lambda$.

The results in the fourth column in Table 4 satisfy the condition

$$1-\mathbf{v}_{1(n_k)}\cdot\mathbf{v}_{1(n_k-1)} < \epsilon_2 = 10^{-5}. \tag{C.2}$$

The results obtained for $n_2 = 10$ are taken as the solution of the CLE for the considered load increment $\Delta\lambda$. Table 4 shows an improvement of the relative accuracy for n_3 and a deterioration for n_4, indicating the beginning of numerical problems if the increment was further refined. Modifications of the described procedure, such as e.g. reductions of the load steps, allow treatment of exceptional situations where this procedure might not be sufficiently accurate.

Fig. 34 shows a flowchart concerning the numerical determination of $\dot{\mathbf{K}}_T(\mathbf{q})$ and $(\lambda_{1(j)}-\lambda, \mathbf{v}^*_{1(j)})$ for an arbitrary increment $\Delta\lambda$. Initially, data files and results that were obtained with the help of MSC.MARC in the framework of nonlinear FE analysis are called.

References

[1] P. Helnwein, Zur initialen Abschätzbarkeit von Stabilitätsgrenzen auf nichtlinearen Last-Verschiebungspfaden elastischer Strukturen mittels der Methode der Finiten Elemente [in German; On *ab initio* assessability of stability limits on nonlinear load–displacement paths of elastic structures by means of the finite element method] (Ph.D. thesis), Vienna University of Technology, 1996.

[2] H.A. Mang, G. Hofstetter, Festigkeitslehre [in German; Strength of Materials], fourth ed., Springer, Vieweg, 2013.

[3] H.A. Mang, Categorization of buckling by means of spherical geometry—application to the Austrian Science Fund (FWF) for financial support of a research project, 2011.

[4] R.H. Gallagher, H.T.Y. Yang, Elastic instability predictions for doubly-curved shells, in: Proceedings of the Second Conference on Matrix Methods in Structural Mechanics, Wright-Patterson Air Force Base, Ohio, New Jersey, USA, 1968, pp. 711–739.

[5] B. Brendel, Geometrisch nichtlineare Elastostatik [in German; Geometrically nonlinear elastostatics] (Ph.D. thesis), Institute for Structural Mechanics, University of Stuttgart, Stuttgart, 1979.

[6] E. Ramm, Strategies for tracing the nonlinear response near limit points, in: W. Wunderlich, E. Stein, K.J. Bathe (Eds.), Nonlinear Finite Element Analysis in Structural Mechanics, Springer, 1981, pp. 63–89.

[7] H.A. Mang, G. Höfinger, Bifurcation buckling from a membrane stress state, Internat. J. Numer. Methods Engrg. 90 (7) (2012) 867–881.

[8] H.A. Mang, X. Jia, G. Höfinger, Finite element analysis of buckling of structures at special prebuckling states, J. Theoret. Appl. Mech. 50 (3) (2012) 785–796.

[9] O.C. Zienkiewicz, R.L. Taylor, The finite element method, fifth ed., in: Solid Mechanics, vol. 2, Butterworth-Heinemann, 2000.

[10] A. Steinboeck, G. Höfinger, X. Jia, H.A. Mang, Three pending questions in structural stability, J. Int. Assoc. Shell Spat. Struct. 50 (1) (2009) 51–64.

[11] C.R. Wylie, Advanced Engineering Mathematics, fourth ed., McGraw-Hill, 1975.

[12] MSC Software Corporation, Santa Ana, CA 92707. Marc Manual Volume B: Element Library, 2012.

[13] X. Jia, FE_{v2} Finite Element Software Written in MATLAB, Technical University of Vienna, 2012.

[14] X. Jia, H.A. Mang, Assessment of solutions from the consistently linearized eigenproblem by means of finite difference approximations, Comput. Struct. 151 (2015) 42–48.

[15] R. Kindmann, Stahlbau: Teil 2: Stabilität und Theorie II. Ordnung [in German; Steel Construction: Part 2: Stability and Theory of Second Order], fourth ed., Ernst, Berlin, 2008.

[16] T.F. Banchoff, S.T. Lovett, Differential Geometry of Curves and Surfaces, Taylor & Francis, 2010.

[17] H.A. Mang, C. Schranz, P. Helnwein, Conversion from imperfection-sensitive into imperfection-insensitive elastic structures. I. Theory, Comput. Methods Appl. Mech. Engrg. 195 (13–16) (2006) 1422–1457.

[18] C. Schranz, B. Krenn, H.A. Mang, Conversion from imperfection-sensitive into imperfection-insensitive elastic structures. II. Numerical investigation, Comput. Methods Appl. Mech. Engrg. 195 (13–16) (2006) 1458–1479.
[19] X. Jia, H.A. Mang, Conversion of imperfection-sensitive elastic structures into imperfection-insensitive ones by adding tensile members, J. Int. Assoc. Shell Spat. Struct. 52 (2) (2011) 121–128.
[20] MSC Software Corporation, Santa Ana, CA 92707. Marc Manual Volume A: Theory and user information, 2012.
[21] X. Jia, H.A. Mang, Determination of the derivative of the tangent stiffness matrix with respect to the load parameter, PAMM 13 (1) (2013) 119–120.
[22] W.T. Koiter, On the stability of elastic equilibrium. NASA technical translation. National Aeronautics and Space Administration, 1967.
[23] S. Pavlicek, Die Beulkugel. Eine Symbiose von Mechanik und Geometrie [in German; The buckling sphere: A symbiosis of mechanics and geometry] (Ph.D. thesis), Technical University of Vienna, 2016.